Liquid metal embrittlement cracking in dissimilar resistance spot welding of 3rd Gen – Advanced high strength steel: mitigation methods and associated mechanisms

by

Meet Patel

A thesis

presented to the University of Waterloo

in fulfillment of the

thesis requirement for the degree of

Master of Applied Science

in

Mechanical and Mechatronics Engineering

Waterloo, Ontario, Canada, 2022

© Meet Patel 2022

Author's Declaration

This thesis consists of material all of which I authored or co-authored: see Statement of Contributions included in the thesis. This is a true copy of the thesis, including any required final revisions, as accepted by my examiners.

I understand that my thesis may be made electronically available to the public.

Statement of Contributions

This thesis was solely written by the candidate. Professor E. Biro contributed to editing the entire thesis. Additional contributions were made by other members of the Centre of Advanced Material Joining research group. Specific contributions to this work, other than those already noted, are listed below.

Professor Elliot Biro supervised the research progress and guided on research direction, reviewed manuscripts, and provided valuable input through technical discussions.

Dr. H. Ghassemi-Armaki from General Motors (GM), Michigan, USA acted as an industrial supervisor, provided feedback on research direction and edited manuscripts.

Chapter 5 of this thesis is based on a journal paper which has been submitted in the Journal of Manufacturing Process.

M. Patel, M. Shojaee, O. Sherepenko, A.R.H. Midawi, H. Ghassemi-Armaki, E. Biro, "Mitigating the influence of industrially relevant disturbances on LME severity of dissimilar resistance spot welded advanced high-strength steels."

The experimental work, analysis of experimental data, and writing were conducted solely by the candidate. The candidate was the primary author of the paper. Mohammad Shojaee and Oleksii Sherepenko assisted in performing welding process, Abdelbaset R.H. Midawi assisted in testing the mechanical properties of the as-received material. Dr. H. Ghassemi-Armaki and Prof. Biro's role were as described above.

Chapter 5 of this thesis is based on a journal paper which is being prepared.

M. Patel, J.U. Kim, O. Sherepenko, E. Biro, “Mechanisms responsible for lowering LME severity of dissimilar resistance spot welded advanced high-strength steels.”

The experimental work, analysis of experimental data, operation of ESI Sysweld® simulation software, and writing were conducted solely by the candidate. The candidate was the primary author of the paper. JiUng Kim assisted in setting up infrared camera, Oleksii Sherepenko assisted in creating electrode mesh for simulation, and Prof. Biro’s role was as described above.

Abstract

In response to the automotive industries demands for safer, lighter, and more environmentally friendly vehicles, the third generation of advanced high-strength steels (3G-AHSS) has been developed to have both high strength and high ductility. To protect these materials from corrosion during service, these materials are typically coated with zinc. During resistance spot welding (RSW), the zinc coating can melt, allowing it to penetrate into the grain boundaries (GBs), and lead to liquid metal embrittlement (LME) cracking when combined with tensile stresses associated with the RSW process. Several possible strategies for lowering LME severity by altering welding parameters have been proposed in the literature, but these strategies have been predominantly focused on similar joints. However, as the vast majority of welds in automotive construction join materials of different thicknesses and grades, dissimilar weld performance is also of interest. Therefore, it is also of interest to understand how LME changes in dissimilar joints as compared to similar joints, as well as whether methods to reduce LME severity must take the dissimilar nature of the joint into account to improve weld quality.

In this work, a 3G-AHSS galvanized (GI-coated), known to be highly susceptible to LME, with a nominal sheet thickness of 1.4 mm was welded, both to itself and to a 0.6 mm thick Interstitial Free (IF) steel. The effect of joint construction on LME cracking severity was determined by comparing the cracks resulting from welds made in both similar material and dissimilar material joints. It was found that differences in material characteristics, between the two materials, resulted in differences in temperature distribution in the similar and dissimilar joints, causing high LME severity in the dissimilar joint.

An industrially viable welding schedule was developed to minimize the LME severity in dissimilar joints. The severity of the LME cracks that formed in welds made using the developed weld

schedule was compared to those developed in welds made with baseline welding parameters, resulting in a 46% reduction in a severity of LME cracking. The mechanism of LME reduction was analyzed using the finite element modeling software Sysweld®. The obtained results were compared with in-situ thermography using an infrared camera. It was observed that the difference in a thermal gradient and the distance between the fusion boundary and electrode/sheet interface are responsible for LME severity.

The robustness of the developed welding schedule was then tested on welds made with typical industrial disturbance factors such as pre-strained sheets (between 0 to 80% of material yield strength) and electrode misalignment (between 0° to 10° misalignment) compared to baseline parameters. When welds were made in joints affected by severe disturbance factors, the resulting optimized welding schedule decreased LME cracking and showed improved resistance to LME, lowering LME severity by 41% for the extreme pre-strain condition and 27% for the extreme misalignment angle.

Acknowledgments

Words cannot express my deepest gratitude to my supervisor, Prof. Elliot Biro for his time, advice, guidance, and invaluable feedback throughout the journey of my master's study, who generously provided knowledge and expertise. I would also like to thank my committee members for letting my seminar be an enjoyable moment, and for your comments and suggestions.

Secondly, this endeavor would not have been possible without the generous support from Mr. Eric McCarty who managed the project at the Auto Steel Partnership (A/SP), who provided the material and financed my research.

I am also grateful to my colleagues in the CAMJ research group, especially Dileep Ramachandran, Olakunle Betiku, Mohammad Shajoee, JiUng Kim, A.R.H. Midawi, and Oleksii Sherepenko for their editing help and long hours of discussion on unexpected results. I enjoyed every day at the office and all the lunchtime debates with you guys.

Lastly, I could not have undertaken this journey without the support of my family, especially my parents, Sandip Patel and Harshika Patel, who always stood by my side throughout my academic journey. Thanks should also go to my cousin Vikas Patel who impacted and inspired me.

Table of Contents

Author's Declaration ii

Statement of Contributions iii

Abstract v

Acknowledgments vii

List of Figures xiii

List of Tables xvi

List of Abbreviations xvii

Chapter 1 Introduction 1

1.1 Background 1

1.2 Objectives 1

1.3 Thesis Outline 2

Chapter 2 Literature Review 4

2.1 Advanced High Strength Steel (AHSS) 4

2.1.1 Quench and Partitioned (Q&P) Steel 6

2.2 Zinc Coatings 7

2.2.1 Hot-dip Galvanization 8

2.2.2 Electrogalvanization 8

2.3 Resistance Spot Welding (RSW) 8
2.3.1 RSW Fundamentals 9
2.3.2 Welding Parameters 13
2.3.3 Weld Lobe 14
2.3.4 Pulsed Welding Schedule 15
2.4 Dissimilar Welding 17
2.5 Liquid Metal Embrittlement (LME) 18
2.5.1 Influence of Temperature 20
2.5.2 Effect of Material Strength on LME 22
2.6 LME in RSW of AHSS 23
2.6.1 Classification of LME Cracks during RSW 24
2.6.2 Influence of Weld Parameters on LME 24
2.6.3 The Influence of LME on Weld Mechanical Performance 26
2.6.4 LME in Dissimilar Joint 26
2.6.5 Methods for Suppressing LME in RSW 28
Chapter 3 Methodology 31
3.1 Materials 31
3.2 Resistance Spot Welding 33

3.3 Selection of Baseline Welding Parameters 34

3.4 Welding Process Simulation 37

3.5 In-situ Monitering of Spot Welding Process 38

3.6 Manufacturing Variability 39

3.7 Metallography and Microscopy 41

3.8 LME Severity Measurement 42

Chapter 4 LME Cracking Severity in Similar and Dissimilar Joint 44

4.1 Difference in Cracking Index for Similar and Dissimilar Joint 44

4.2 Temperature Distribution in Similar and Dissimilar Joint 46

4.3 Quantification of Distance between Fusion Boundry and Electrode/Sheet Interface. 47

4.4 FEM Analysis of Temperature Distribution for Similar and Dissimilar Joint 48

4.5 Influence of Material Characteristics on Temperature Distribution 49

4.6 Simulation of Temperature Distribution throughout the Welding Process 52

4.7 Summary 54

Chapter 5 Mechanism of LME Exasperation and Welding Parameters Validation 56

5.1 Welding Parameters Optimization for LME Reduction 56

5.2 Mechanism Associated with the LME Reduction 59

5.3 Validation of Simulation Results with IR Thermography 62

5.4 Nugget Movement using the Optimized Welding Schedule 63

5.5 Validation of Welding Parameters 65

5.6 Summary 69

Chapter 6 Conclusions and Future Work 71

6.1 Conclusions 71

6.2 Future Work 73

References 74

Appendix 86

List of Figures

Figure 2.1: Steel strength ductility diagram, illustrating the wide range of properties from AHSS grades [9]. 4

Figure 2.2: Two different regions of automotive structure [10]. 5

Figure 2.3: Q&P steel microstructure obtained using (a) scanning electron microscopy and (b) light optical microscopy. *M* martensite, *F* ferrite, *RA* retained austenite [15]. 7

Figure 2.4: Process steps of the resistance spot welding process [22]. 9

Figure 2.5: Schematic of relative electrical resistance in RSW process [24]. 10

Figure 2.6: Dynamic resistance during the RSW process [24]. 13

Figure 2.7: A weld lobe curve for the RSW process [24]. 15

Figure 2.8: RSW schedule without pulsing (Single pulse) [35]. 16

Figure 2.9: RSW schedule with two pulses [35]. 17

Figure 2.10: Conditions for the occurrence of liquid Metal Embrittlement [45]. 19

Figure 2.11: Ductility trough of Fe22Mn0.6C TRIP steel [47]. 21

Figure 2.12: Stress-strain curves for Fe22Mn0.6C TRIP steel at a) 600°C and b) 800°C [47]. 21

Figure 2.13: Phase diagram of Fe-Zn binary system [16]. 22

Figure 2.14: (a) As welded sample and (b) cross-sectional view of LME cracks in Zinc coated TRIP steel [53]. 23

Figure 2.15: Schematic diagram showing different types of LME cracks according to the location of occurrence 24

Figure 2.16: (a) Two sheet stack-up and (b) Three sheet stack-up used for LME severity evaluation [62]. 27

Figure 3.1: Engineering stress-strain curve for a) GI coated 3G-980 and b) IF steel materials used in this study..... 32
Figure 3.2: Resistance spot welding robot. 34
Figure 3.3: Comparison of nugget penetration between (a) AWS and (b) baseline welding schedules. 35
Figure 3.4: Material properties for RSW (a) Electrical resistivity, (b) density, (c) Heat capacity, and (d) Thermal conductivity 38
Figure 3.5: In-situ measurement of spot-welding process using IR camera..... 39
Figure 3.6: Schematic representation a) Electrode Misalignment and b) Coupon dimension used for pre-strain welding..... 41
Figure 3.7: LME crack length measurement form surface opening to crack root. 42
Figure 3.8: Schematic diagram showing different types of LME cracks according to the location of occurrence. (Reproduced from Figure 2.15) 43
Figure 4.1: LME severity in similar vs dissimilar joint. 45
Figure 4.2: Weld cross-section showing FB for (a) similar joint and (b) dissimilar joint. 46
Figure 4.3: Quantification of distance between fusion boundary and electrode/sheet interface measured for five weld replicates. 47
Figure 4.4: Weld Simulation showing Fusion Boundary for (a) Similar Joint and (b) Dissimilar Joint 49
Figure 4.5: Electrical Resistivity of 3G-980 and IF steel. 50
Figure 4.6: Thermal Conductivity of 3G-980 and IF Steel. 51
Figure 4.7: Temperature distribution in a similar joint at various time intervals. 53
Figure 4.8: Temperature distribution in a dissimilar joint at various time intervals. 54

Figure 5.1: LME cracking index in baseline and optimized welding schedule. 58
Figure 5.2: Low magnification optical images of (a) baseline and (d) optimized schedule showing spot weld cross sections. The higher magnification images illustrate LME cracks in different regions of the corresponding cross-sectional view. 59
Figure 5.3: Validation of FB between experimental results and simulation results for (a) baseline welding schedule and (b) optimized welding schedule. 61
Figure 5.4: Surface temperature during welding cycle at (a) weld indent area using baseline schedule (b) weld indent area using optimized schedule (c) weld shoulder area using baseline schedule and (d) weld shoulder area using optimized schedule. 62
Figure 5.5: Result of fusion boundary location comparison between Sysweld® simulation and an IR camera for (a) baseline welding schedule and (b) optimized welding schedule. 63
Figure 5.6: Quantification of Nugget Movement with Optimized Schedule compared to Baseline Schedule. 64
Figure 5.7: Comparison of (a) Total Cl, (b) Type A CI, and (c) Type B CI resulting from welds made with electrode misalignment for both the standard and optimized weld schedules. 67
Figure 5.8: Comparison of (a) Total Cl, (b) Type A CI, and (c) Type B CI for welds made on a sheet loaded under tension using both the standard and optimized weld schedules. 69

List of Tables

Table 3.1: Test Materials chemical composition. 32

Table 3.2: Test Materials Mechanical Properties 32

Table 3.3: RSW process parameters utilized in this investigation for a dissimilar joint. 36

Table 3.4: RSW process parameters utilized in this investigation for a similar joint. 36

List of Abbreviations

3G-AHSS	Third generation advanced high strength steel
AC	Alternating Current
AHSS	Advanced high strength steel
AWS	American welding society
BIW	Body-in-white
C_{eq}	Carbon equivalent
CFB	Carbide free bainite
DP	Dual phase
EG	Electrogalvanized
EL	Elongation
E/S	Electrode/sheet
FB	Ferritic-bainitic
FEA	Finite element analysis
FEM	Finite element model
GA	Galvannealed
GI	Galvanized
HDGA	Hot-dip galvannealed
HDGI	Hot-dip galvanized
IF	Interstitial free
IR	Infrared
LME	Liquid metal embrittlement
LCS	Low carbon steel
MFDC	Medium frequency direct current
MWS	Minimum weld size
Q&P	Quench and partition
RSW	Resistance spot welding

SEM	Scanning electron microscope
TRIP	Transformation induced plasticity
TWIP	Twinning induced plasticity
UTS	Ultimate tensile strength
YS	Yield strength

Chapter 1 Introduction

1.1 Background

In 1974, at Nypro Chemical Plant, Fllixborough, England, a fire caused by a mechanical failure in a large reactor vessel led to the severe injuries of thirty-six workers and the death of twenty-eight workers. This mechanical failure was triggered by a cracking and that cracking was caused by a phenomenon known as liquid metal embrittlement (LME) [1]. Liquid metal embrittlement is a phenomenon where certain ductile metals undergo a drastic change in their tensile strength or exhibit brittle fracture when exposed to specific liquid metals [2]. Liquid metal embrittlement during automotive production is also a safety concern. There are several welding processes used to join automotive body-in-white (BIW) structures, but the most commonly used process is resistance spot welding (RSW). When automotive materials are subjected to welding, sometimes causing liquid metal embrittlement. This phenomenon can also result in the degradation of the mechanical performance of the welded joint [3]. Although there has been significant study effort into LME during RSW in recent years, there are still concerns about what types of automotive steels are prone to LME and the extent to which the mechanical performance of the weld is affected. This ambiguity raises safety concerns for automakers. Nowadays, dissimilar welding is commonly used in automobile industries to join body-in-white structural components (thick material) with skin components (thin material). As a result, research is still ongoing to better understand the cause of such severe LME cracking during the RSW process and methods to suppress it.

1.2 Objectives

The goal of this thesis is to investigate the occurrence of LME cracking and its mechanism during dissimilar resistance spot welding of AHSS and provide an industrially viable solution to suppress LME. The specific objectives are as follows:

1. Characterize the differences in LME susceptibility between similar and dissimilar RSW joints.
2. Understands the mechanisms resulting in any observed differences in LME severity between similar and dissimilar RSW joints.
3. Develop welding parameters to reduce LME severity in dissimilar RSW joints.
4. Validate the low LME parameters developed for dissimilar joints on industrially relevant welding situations.

1.3 Thesis Outline

This thesis is divided into six chapters, which are detailed in the following paragraphs.

Chapter 1 gives an introduction to the thesis, containing background, objectives, and constraints of the thesis work.

Chapter 2 summarizes published literature on topics relevant to the thesis including AHSS, RSW, and LME. It also demonstrates gaps in the literature that the thesis work is intended to fill.

Chapter 3 explains the material, experimental and simulation procedure, and analysis methods used to fulfil the objective

Chapter 4 identifies the difference in LME susceptibility of similar and dissimilar joints and explores the possible causes.

Chapter 5 describes the mechanism responsible for reducing the LME in dissimilar joint. It also validate the experimental result with FEA simulation model. Finally, it explores the effect of typical industrial disturbance factors on LME.

Chapter 6 summarizes the main findings of this work. It also states the further questions that are brought up by this study that were identified and need further examination.

Chapter 2 Literature Review

2.1 Advanced High Strength Steel (AHSS)

Reduced fuel consumption is proven as an effective method to lessen the impact of a greenhouse on the environment. [4,5]. One proposed solution for reducing fuel consumption is to reduce the weight of automotive body assemblies. It is important to note that any weight reduction of body assembly should not compromise passenger safety [6,7]. The simultaneous pursuit of vehicle weight reduction and maintaining the crashworthiness of car body assemblies has resulted in the increased interest in advanced high-strength steels (AHSS) [5,8]. A group of steels known as "advanced high strength steels" (AHSS) have unique microstructures and metallurgical properties that use complex deformation and phase transformation processes to achieve very high strength. As shown in Figure 2.1, various types of AHSS are capable to achieve a variety of strength and ductility.

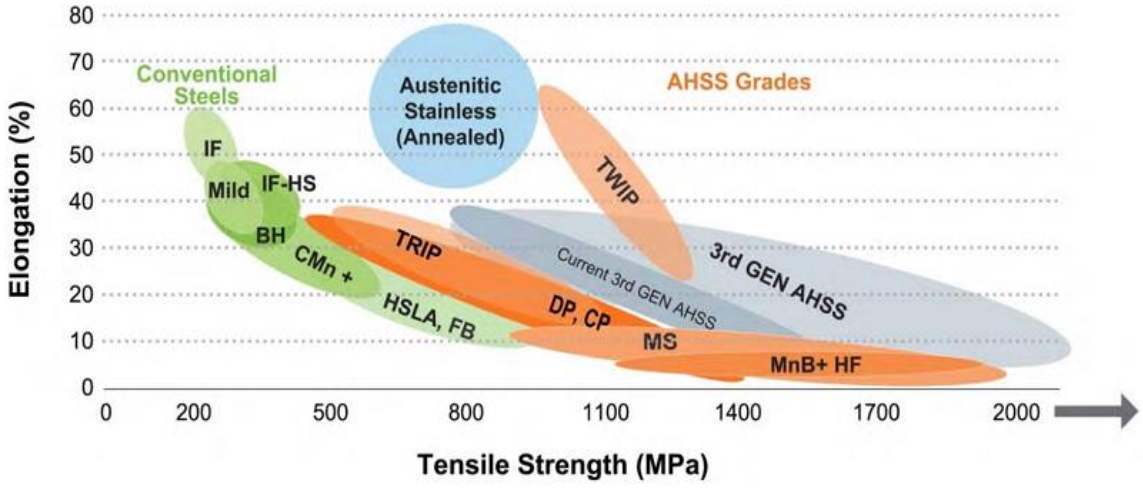


Figure 2.1: Steel strength ductility diagram, illustrating the wide range of properties from AHSS grades [9].

The AHSS studied in this thesis is quench and partitioned steel (Q&P) steel, due to interest from industry. The characteristics of different AHSS steels will be discussed in the following sections. Passenger cars are divided into two distinct areas, each with its own set of safety regulations as shown in Figure 2.2. The front and rear ends of the vehicle is known as “crumple zones”. The crumple zone or areas of the body structure is designed to manage dynamic loads and preserve the structure of the passenger compartment during front and rear vehicle crash event [10]. Q&P steels are ideal for this application because they exhibit high work-hardening rates, strength and ductility compared to conventional high strength steel (HSS) and provides significant stretch-forming capability [9–11].

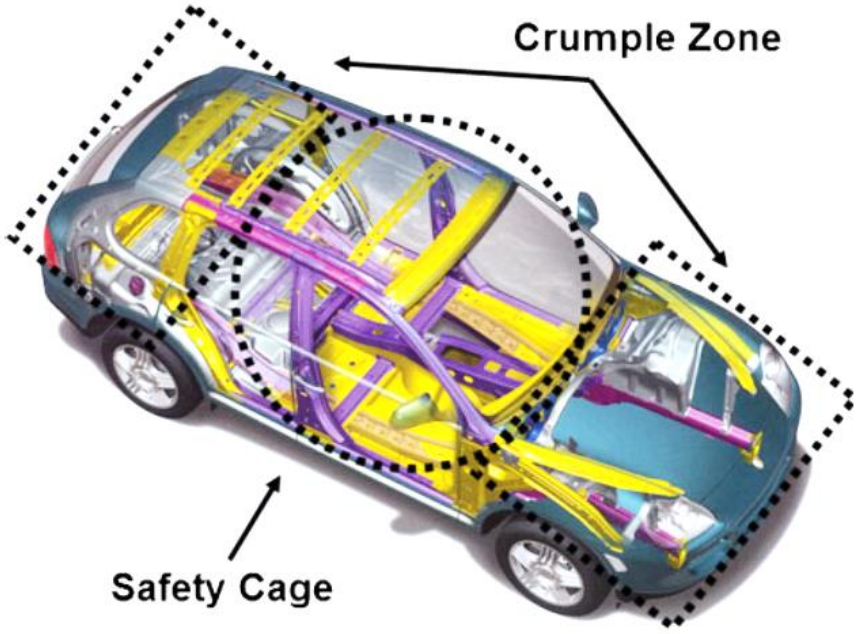


Figure 2.2: Two different regions of automotive structure [10].

The second region is vehicle’s safety cage, which is designed to transfer loads without buckling to prevent intrusion that may impinge the space around the passenger and protect vehicle occupants

during crash event. Hot-formed, martensitic, and complex-phase steels (not discussed in this thesis) are used for this application since they exhibit very high yield strength [9–11].

2.1.1 Quench and Partitioned (Q&P) Steel

The purpose of using Q&P steel in vehicle construction is to create a new type of ultrahigh-strength steel to obtain higher ductility (10-20%) to increase fuel efficiency while enhancing passenger safety [11]. The commercial Q&P steel has a microstructure mainly consisting of martensite (50-80%) formed during quenching and ferrite (20-40%) formed from the austenite phase during slow cooling, as well as dispersed retained austenite (5-10%) stabilized by carbon enrichment during partitioning as shown in Figure 2.3 [11–13]. Similar to traditional TRIP steel, Q&P steel has a chemical composition that includes 0.2% C and other alloying elements (1-1.5% Al, 1-1.5% Mn) to stabilize its retained austenite at room temperature [12,13]. It has been shown that Q&P steel exhibited ultrahigh strength due to the martensite laths, and it was found that its good ductility was a result of the TRIP-assisted behavior of the retained austenite during deformation [11]. Similar to TRIP steel, during deformation, the dispersed retained austenite progressively transforms to harder martensite, which improves the work-hardening and ductility of the Q&P steel [14,15].

Q&P steel is manufactured by first heat treating it so that the material is either fully or partially austenitized. This is followed by interrupted quenching of the steel to a temperature in between martensite-start and martensite-finish temperature which results in untransformed retained austenite and martensite[12,13]. During the partitioning step, the quench steel is held either at or above the initial quench temperature. In this step, carbon partitions from martensite into the austenite stabilize the austenite at the room temperature [12,13]. Figure 2.3 shows the final microstructure of Q&P steel containing martensite, ferrite, and retained austenite.

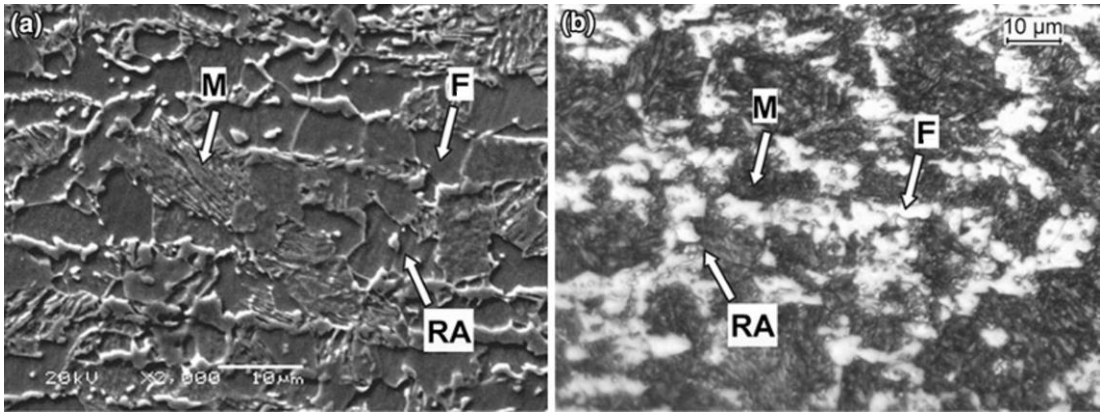


Figure 2.3: Q&P steel microstructure obtained using (a) scanning electron microscopy and (b) light optical microscopy. *M* martensite, *F* ferrite, *RA* retained austenite [15]**.**

2.2 Zinc Coatings

AHSS used in automotive manufacturing are typically coated with zinc to protect against corrosion. Zinc coating protect the underlying steel in two ways [16]:

1. Barrier protection –The steel is protected from corrosion by zinc coating because the coating isolates the steel and act as a protective barrier, keeping air and moisture out and preventing oxidation.

2. Galvanic protection – At ambient conditions, zinc is anodic to iron and will corrode sacrificially to preserve the substrate steel, even if some of the steel is exposed as cut edges or scratches in the coating.

There are two types of zinc coatings typically used in the automobile industry: hot-dipped and electrogalvanized [9].

2.2.1 Hot-dip Galvanization

In hot-dip galvanization, the steel or iron is immersed in a bath of molten zinc. To promote adhesion, the steel is pre-heated to a temperature that is similar to that of a zinc bath. To achieve the necessary coating thickness after dipping, the extra zinc is removed the surface with air knives [9,16,17]. To brighten the initial coating appearance, 0.005-0.02 wt% of aluminum is added to the zinc bath [16]. This type of coating referred to as hot-dip galvanized (HDGI or GI) coating.

The coating may be annealed at a temperature of 450-600°C after hot-dip galvanization [16,18]. This enables iron to diffuse into the zinc coating and produce an iron-zinc alloy. After annealing process the coating generally contains 8–12% iron [9,16,18]. This type of coating is referred to as hot-dip galvannealed (HDGA or GA).

2.2.2 Electrogalvanization

Electrogalvanization is another commonly used technique for applying the zinc coating. This technique involves electroplating the zinc onto a steel substrate [9,16]. It is possible to produce pure zinc coatings that are thinner, more aesthetically appealing, and requires less temperature for processing [9]. These coatings are referred to as electrogalvanized (EG) coatings.

2.3 Resistance Spot Welding (RSW)

Resistance spot welding (RSW) is a fusion welding process in which the sheet to be joined are stacked together in a lap configuration, and the workpiece is melted by resistive heating generated by passing an electrical current through the workpiece [10,19,20]. RSW is easy to operate, low cost and low cycle time, making RSW most widely used joining method in the automotive industry. Typically, there are about 2000-5000 spot welds in modern vehicle [10,21].

2.3.1 RSW Fundamentals

The five stages of the RSW process are shown in Figure 2.4 [22] :

1. Two or more sheets are clamped between two water-cooled copper alloy electrodes.
2. The full electrode force is applied to the sheets for a set amount of time.
3. An electric current is passed through the clamped joint to generate the heat for predetermined amount of time.
4. The current is terminated, and the sheets are held under the electrode force to allow the weld to cool and solidify.
    - The amount of time for which the electrode remains in contact with the workpiece while still applying the force is known as the holding time.
5. Electrode force is released.

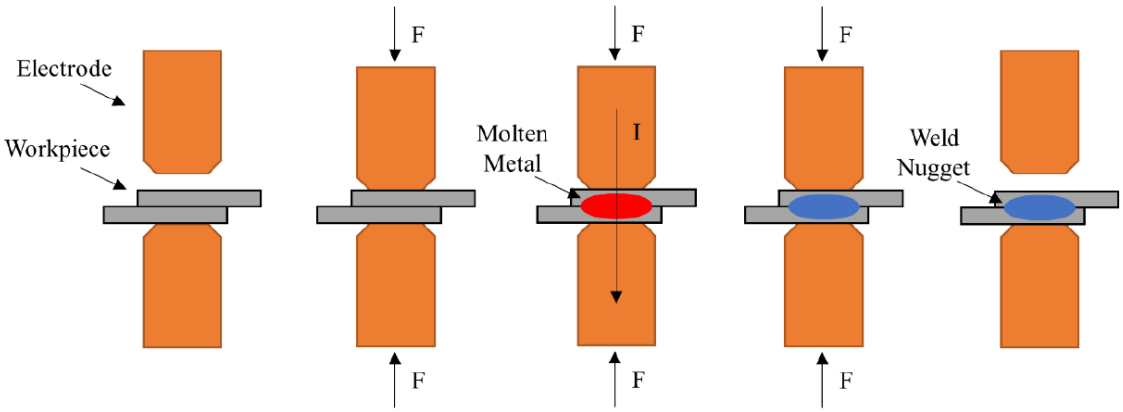


Figure 2.4: Process steps of the resistance spot welding process [22].

The resistance spot welding process produces the required heat for welding through what is known as Joule heating as shown in equation (2.1). Where, Q is the amount of heat produce, I is the current applied, R is the resistance between the electrode, and t is the duration of the applied current [23].

$$Q = \int I^2 R \mathrm{d}t \tag{2.1}$$

The total resistance R is composed of seven individual resistance that exist in the circuit as shown in Figure 2.5. R_1 and R_7 represent the bulk resistance of the copper electrode, R_2 and R_6 represent the contact resistance between the electrodes and the sheets, R_3 and R_5 represents the bulk resistance of the sheets, and R_4 represents the contact resistance between the sheets [24]. Since these resistances are in series, R can simply be calculated by summing them. A sheet-to-sheet interface generally generates the most heat during the welding process since R_4 has the highest resistance [25].

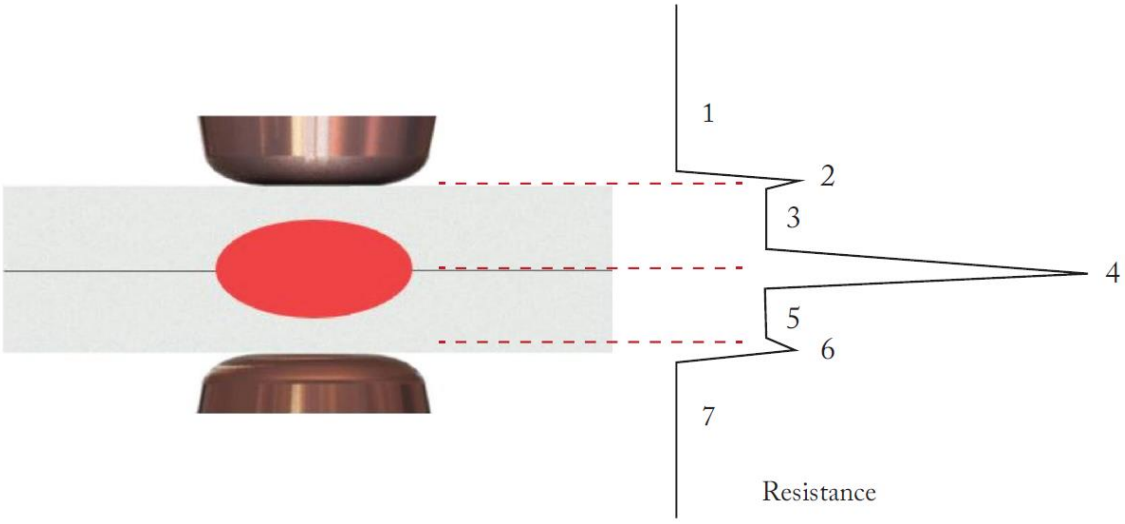


Figure 2.5: Schematic of relative electrical resistance in RSW process [24].

The resistance fluctuates during the welding cycle as the material is heated and melted due to difference in temperature. The overall resistance is a combination of various contact and bulk resistance in the joint during the welding cycle, the dynamic resistance. The dynamic resistance may be calculated using the measured instantaneous voltage and current. The dynamic resistance has a consistent regions that are representative of changes that occur during the welding cycle. Figure 2.6 shows the dynamic resistance curve during resistance spot welding process. The steps of spot weld formation may be explained using the dynamic resistance curve as follows [26] :

I. Surface breakdown - Under normal conditions, the initial contact resistance is very high due to the presence of oxide layers, surface films, and other contaminants. Therefore, when current begins to flow, the initial generation of heat is concentrated at the surfaces. This heat will result in a breakdown in the surface contaminants, leading to a very sharp drop in resistance [26].

II. Asperity collapse – In this stage, metal-to-metal contact exists. However, the surface resistance may still remain relatively high because the effective contact is limited due to surface roughness. These asperities will soften as the metal heats, increasing temperature as well as contact surface and lowering resistance even further. Additionally, increasing temperature causes resistivity to increase, which will have the opposite effect. Resistance increases or decreases is determined based on the competition between these two mechanisms, thereby determining the position of α trough, the point where resistance first ceases to decreases and starts to increase [26].

III. Heating of the workpieces – In this stage, the temperature of bulk material increases, which increases the bulk resistance, increasing the overall resistance [26].

IV. First melting – Melting starts at the sheet-to-sheet interface. The material's bulk temperature continues to increase, increasing bulk resistance. However, the heat being generated also increases melting at the surface, increasing the cross-sectional area and size of the molten region and causing a decrease in resistance. This stage makes perfect contact at faying surface, as a result the contact resistance falls to zero. The liquid has a much lower resistivity than that of solid metal. Resistance starts to decrease as temperature stabilizes and nugget growth dominates. This point on a curve is referred to as the β peak [26].

V. Molten nugget growth - Beyond the β peak, the resistance decreases further as the nugget continues to grow. The increased temperature softens the metal, causing the electrode to press into it and form an indentation (mechanical collapse). This decreases sheet thickness (current path) and leads to a decrease in resistance. Expulsion (ejection of molten metal from the weld nugget) will occur if the nugget increases to the point that it can no longer be contained by the surrounding solid metal under the compressive electrode force. As a result of expulsion, the resistance decreases sharply [26].

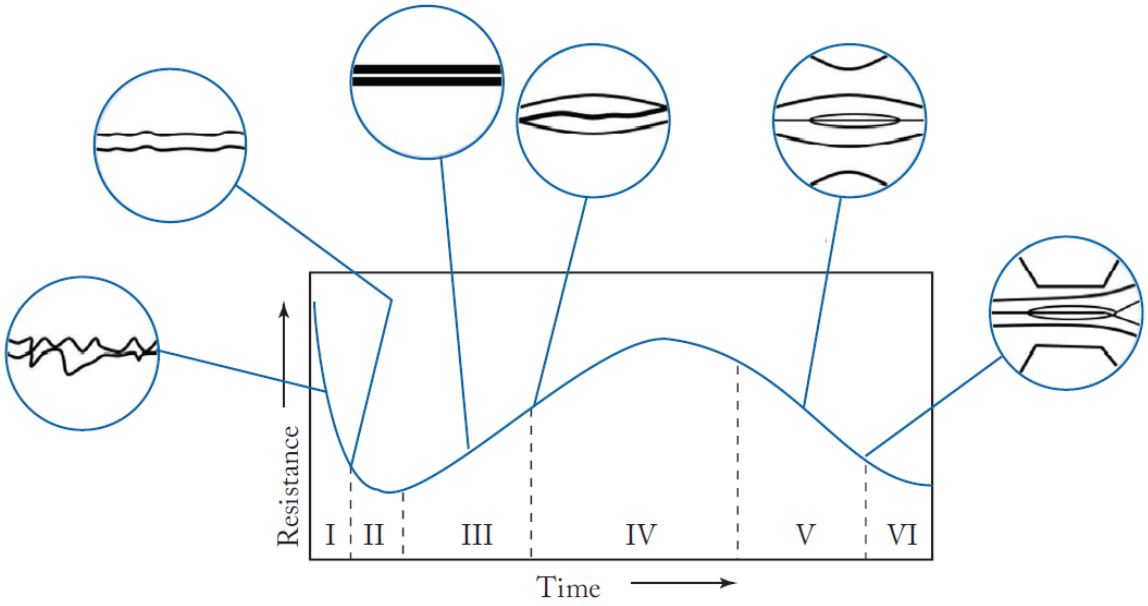


Figure 2.6: Dynamic resistance during the RSW process [24].

2.3.2 Welding Parameters

Many parameters govern the RSW process, mainly welding current, welding time, hold time, electrode force, etc. These parameters control weld heat input and, thus, the nugget diameter of a resultant weld. Weld current, weld time, and electrode force are the most critical parameters since they directly influence nugget size [10,21]. As the weld current and weld time increase while the other parameters remain constant, the heat input increases (Eqs. (2.1)), which increase melting, leading to a larger nugget diameter. The weld force alters the resistance between the electrodes. Since the metal sheets must be forced together to allow the current to flow, the electrode force also influences heat input. A more significant electrode force pushes the sheets closer together, increasing the effective contact area between the two sheets. As well, increased force crushes asperities, putting material in more intimate contact, which reduces nugget diameter and heat input [10,19,21]. During heating, the

weld force also helps keep the molten nugget between electrodes. The molten nugget may expel liquid from the sheet-to-sheet contact if the weld force is insufficient. This phenomenon is referred to as an "expulsion" [10,19,21].

2.3.3 Weld Lobe

The nugget diameter is the most important factor in determining the strength and fracture mode of resistance spot weld [10]. As a result, only a particular nugget diameter range is suitable for engineering applications. The AWS D8.9 standard for RSW [27], which is generally accepted in North America specifies the minimum weld size (MWS) as

$$Minimum\ Weld\ Size = 4\sqrt{t} \quad \textbf{(2.2)}$$

Where t is the thickness of sheet. The average sheet thickness is used when welding dissimilar materials with different sheet thickness. Welds that are undersized are undesirable because it decreases the weld strength. At the same time, the diameter of the nugget cannot be too large. If the nugget diameter exceeds the region being squeezed by the electrode expulsion will result (ejection of molten metal from the weld zone). As shown in Figure 2.7, expulsion is the upper limit of the workable current range. It is undesirable because it could cause defects in the weld nugget and reduce the weld strength [28].

A weld lobe, such as the one illustrated in Figure 2.7, reveals the range of weld current and weld duration that would create acceptable welds in production while also providing a way of quality control through monitoring of these weld parameters. Welding time and current are varied, but other parameters such as weld force and hold duration remain constant. Welding done inside the weld lobe is desirable to produce sufficient nugget size, without expulsion defect. The width and location of the weld lobe are determined by the material properties of the sheets being welded, such as bulk resistivity,

sheet thickness, surface condition, etc [29]. A broader and larger weld lobe is typically considered preferable since it implies that a wider range of parameters can be used to produce an acceptable weld, making the process more tolerant to variations in a production environment [29].

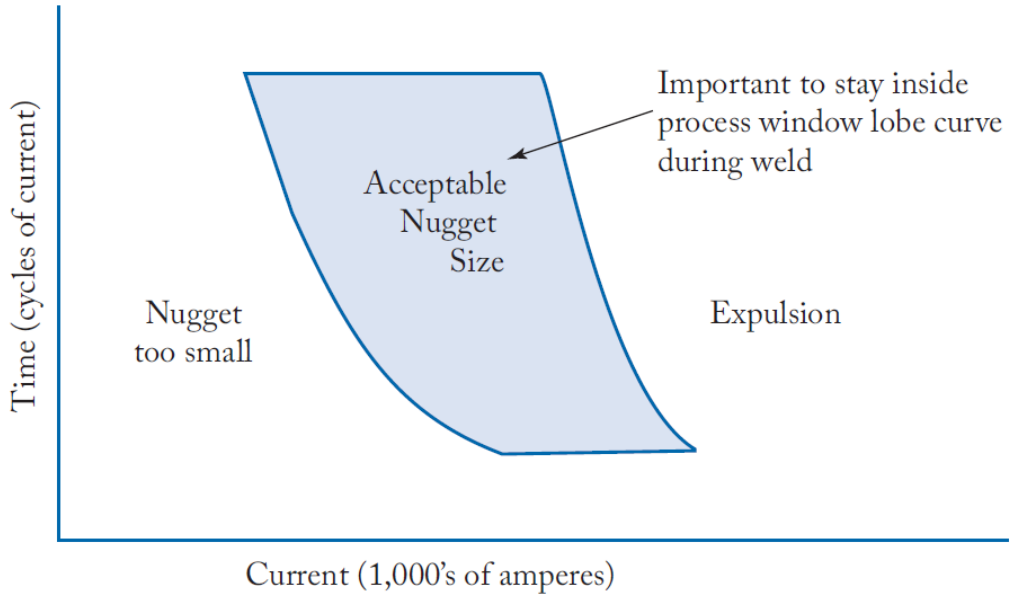


Figure 2.7: A weld lobe curve for the RSW process [24].

2.3.4 Pulsed Welding Schedule

A schematic of welding schedule without pulsing (single pulse) is shown in Figure 2.8. This type of welding schedule is the most basic RSW schedule with constant amount of current and provides approximately constant heat input throughout the welding time [30]. A multiple pulse welding schedule may be beneficial in some cases. Figure 2.9 depicts a pulsed welding schedule that separates the primary welding current into two separate pulses. There is no limit to the number of pluses, the current for

individual pulses, or the cooling time between pulses when developing a pulsed welding schedule. However, pulsed welding schedules often take longer than welding schedules without pulsing because the pulsing introduces cooling time between two pulses which needs to account for total welding time. Hence, it is lengthening the total welding time. Due to this, the total productivity of the pulsed welding schedules is reduced. On the other hand, this approach has been shown to reduce nugget growth rate and delay expulsion, increasing weldable current range [31,32]. This is particularly important when welding AHSS since AHSS have smaller weld lobes than mild and high strength steels [33]. In fact, RSW standards such as AWS D8.9 and the A/SP standard recommend pulsed welding schedules for welding AHSS sheets thicker than 1.3mm [27,34].

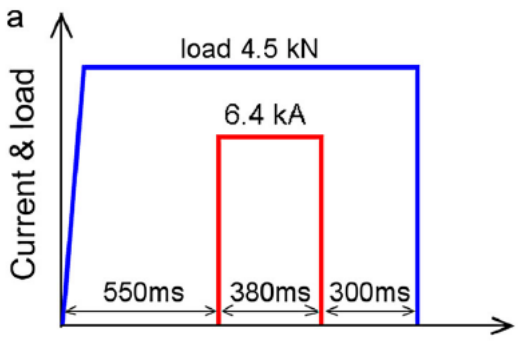


Figure 2.8: RSW schedule without pulsing (Single pulse) [35].

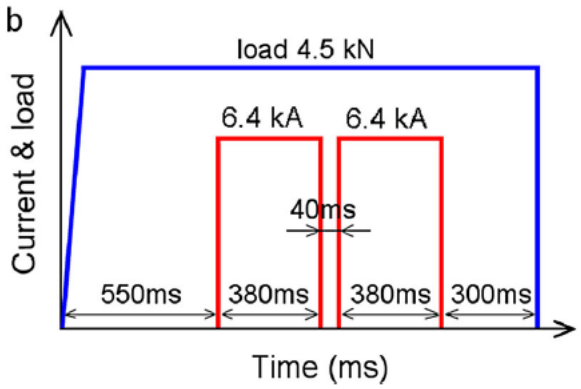


Figure 2.9: RSW schedule with two pulses [35].

2.4 Dissimilar Welding

To improve fuel efficiency and car crashworthiness, advanced high-strength steels (AHSS) are increasingly being used in manufacturing body-in-white (BIW) structures, specifically in structural parts like pillars and rails. However, high-strength materials pose new manufacturing challenges due to their costs, weldability, and formability [36]. Welding of complex stack-ups is one of these challenges which typically consist of two or more than two sheets of similar or dissimilar steels with unequal sheet thicknesses. In automotive applications, a thin sheet with a nominal sheet thickness of 0.6 to 0.8 mm is attached to various metals that go up to 5 to 6 mm thick [36].

When a complex stack-up such as one made up of a thin sheet of low-strength steel is attached to the thick sheet of AHSS, resistance spot welding can be challenging. As a result, heat balance (tendency of nugget shifting towards thicker sheet) becomes a problem when resistance spot welding such stack-up. In such scenario, it can be difficult to attain sufficient penetration into the thin sheet without expulsion on the thick sheet side because the heat loss on the thin sheet side is much faster than on the thick sheet side [36]. Gould *et al.*[36] studied a three sheet stack-up using 0.7-mm-thick low-

carbon steel with 2-mm-thick DP590 and 2-mm-thick DP590. The sheets were welded in two stages by varying electrode force, current, and time to increase melting and penetration into the thin sheet. Their study concluded that by using short overall welding time, the highest penetration was achieved into the thin sheet. This was accomplished by using moderate ratios of forge to weld force as well as higher ratio of forge to weld current. However, the nugget growth mechanism during RSW for a three-sheet stack-up was not investigated.

The nugget formation mechanism is different in dissimilar welding compared to similar welding during RSW process as compared to similar welding. In a resistance spot welding of a three-sheet stack-up using 0.6 mm thick SAE 1004 with 1.8 mm thick SAE 1004 and DP 600, Shen *et al*. [37] investigated the formation mechanism of the weld nugget as well as the influence of different sheet thickness combination on the penetration at the interface of thin sheet to thick sheet and the nugget diameter. It was shown that the nugget first initiated earlier at the thick/thick interface, as opposed to the thin/thick interface. In this study, it was determined that a ratio of top sheet thickness to the bottom sheet thickness should be less than 1:3 to meet the minimum nugget diameter at the thin/thick sheet interface and to achieve at least 20% penetration in the thin sheet [38].

2.5 Liquid Metal Embrittlement (LME)

The liquid metal embrittlement (LME) is a cracking phenomenon that occurs when a solid metal is exposed to liquid metal [39]. LME is the phenomenon whereby a liquid metal diffuses along the grain boundaries of a ductile metal or alloys when stressed. The liquid metal intrusion results in the loss of strength and ductility [3]. This phenomenon is common in certain solid-liquid metal combinations including steel-zinc and copper-mercury [39]. LME is frequently observed during welding when steel is exposed to molten zinc and stress is applied to the solid metal [40]. As a result

of grain boundary decohesion, liquid metal penetrates into the grain boundaries of solid metal. The solid boundary is replaced by liquid film, weakening them and causing surface cracks nucleation [2,41,42]. Tensile stresses can cause these cracks to open up, allowing zinc to penetrate deeper into grain boundaries and propagate the crack [2]. Solid metal does not undergo any bulk chemical or structural changes [3].

Three conditions must be met for LME to happen: a susceptible microstructure (the material that have its strength reduced when the GBs are infiltrated by the liquid metal), liquid zinc in close proximity with solid steel, and tensile stresses [43,44]. Figure 2.10 shows the pre-requisite conditions for LME to occur [45]. For LME to occur, it is necessary for these conditions to exist, but not sufficient [3]; several other factors also contribute to LME occurrence, which are discussed in the following sections.

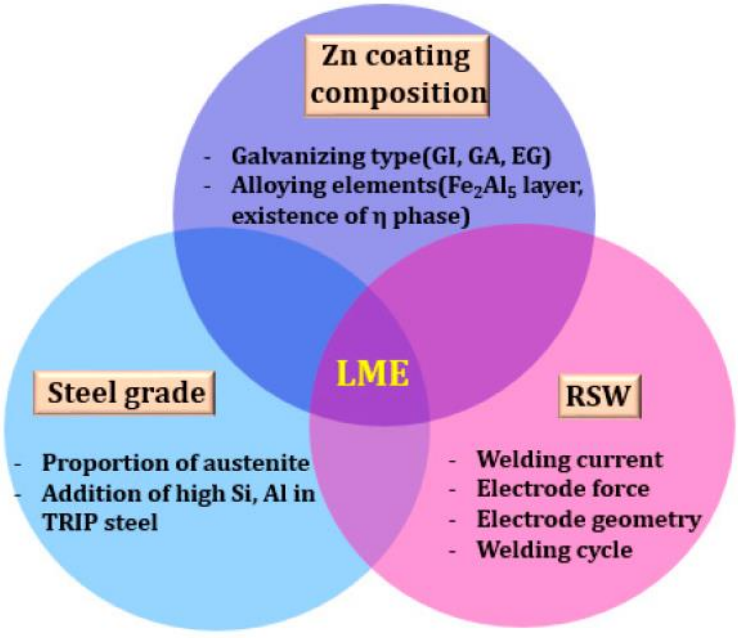


Figure 2.10: Conditions for the occurrence of liquid Metal Embrittlement [45].

2.5.1 Influence of Temperature

LME depends on temperature, and there is a critical temperature range where LME significantly reduces the ductility of the steel. This temperature range is referred to as the "ductility trough" [3]. The ductility troughs can be plotted with respect to fracture energy reduction as ductility reduction leads to a reduction in fracture energy [46]. As shown in Figure 2.11 the ductility trough for a TWIP steel is characterized by the percentage reduction in fraction energy because of early fracture caused by LME. The ductility trough of this TWIP steel begins at 700˚C and ends at 950˚C. LME may not occur immediately following melting, since its onset temperature must be higher than that of the embrittling agent's melting temperature. It has been observed that LME begins around 700 °C in the $steel_{solid}/Zn_{liquid}$ system, well above the temperature where zinc melts at 419 °C [2,42,46–48]. It is generally accepted in literature that the ductility trough typically ends at 950ºC (above liquid Zn boiling point) and prevention of LME formation is due to liquid Zn shortage. The same criterion holds true for other solid/liquid metal system having ductility trough that ends at the boiling temperatures of their embrittling liquids. According to Beal *et al.* [46], the critical stress requires for LME is higher than UTS and YS at the temperature below 700˚C . Due to this, plastic deformation is caused before formation of LME cracks. When the temperature rises over 700ºC, LME cracking occurs before plastic deformation as the critical stress for LME falls below the yield strength and ultimate tensile strength. Beal, however, also noted that experimental methods also heavily influence the LME onset temperature. A comparison of hot tensile experiments on LME using Fe22Mn0.6C TRIP steel is shown in Figure 2.12, which illustrates that the stress-strain curves for bare and electrogalvanized steels were identical at 600°C (Figure 2.12 a), whereas at 800°C the EG coated steel exhibited significant loss of strength and ductility (Figure 2.12 b) [47].

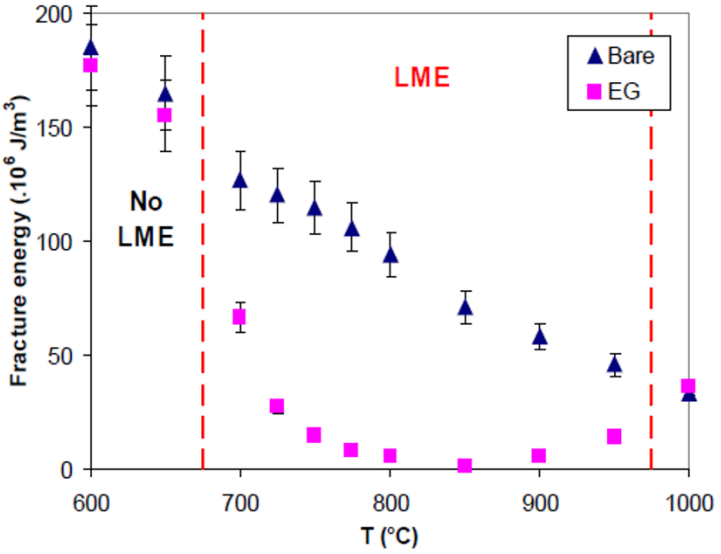


Figure 2.11: Ductility trough of Fe22Mn0.6C TRIP steel [47].

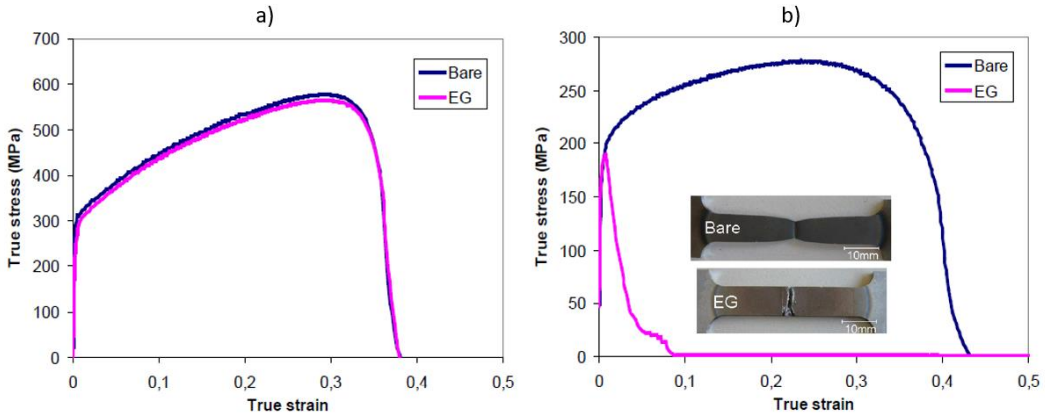


Figure 2.12: Stress-strain curves for Fe22Mn0.6C TRIP steel at a) 600°C and b) 800°C [47].

In a study by Kang *et al.* [49], an intermetallic compound of Fe-Zn was formed during a hot tensile test on Zn-coated steel. As a result, this intermetallic could serve as a barrier between the steel substrate and the liquid zinc. Figure 2.13 shows the Fe-Zn binary phase diagram at 672°C and 782°C,

indicating that between these two temperatures a sufficiently dissolved Γ1 phase may have allowed liquid zinc to make a contact with steel substrate, causing LME to occur. Beal *et al.* [46] noticed that the formation of Fe-Zn intermetallic compounds in EG coated TWIP steel at 750°C prevented LME during high temperature tensile tests. Both Beal and Kang provide reasonable explanations for why LME occurs in Fe-Zn systems at temperatures much higher than Zn melting point.

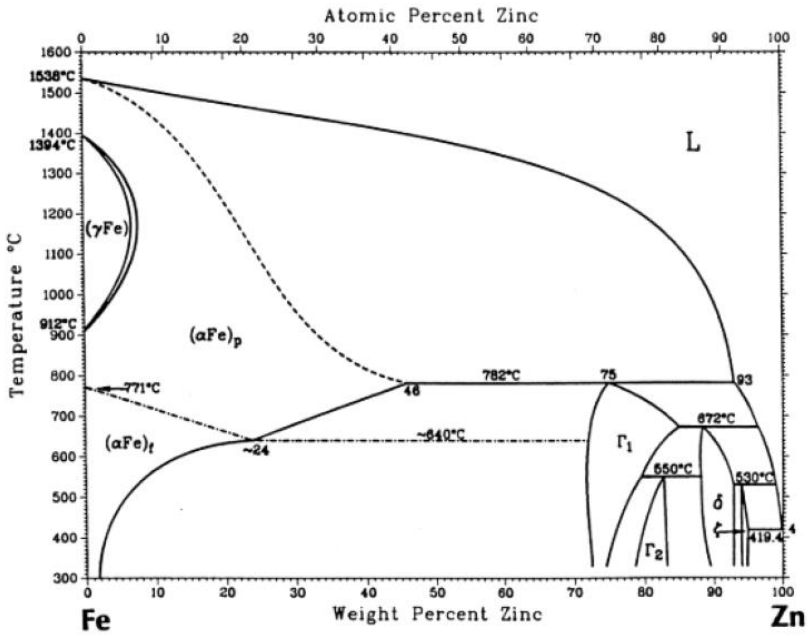


Figure 2.13: Phase diagram of Fe-Zn binary system [16].

2.5.2 Effect of Material Strength on LME

LME susceptibility of the steel is also influenced by the strength of the steel. Steels with higher strength have been found to have wider ductility troughs than steels with lower strength [46]. It has also been found that embrittled steel with a higher strength has a higher LME crack density and deeper crack penetrations than steel with a lower strength [50]. In terms of stress, steels with higher strength are

subjected to higher stresses at the crack tip in comparison with steel with lower strength because higher strength steels are more likely to reach their critical stress levels necessary for initiation of LME as a result of higher stress state in comparison with lower strength steel [49]. As a result of high stresses, the solid-state diffusion and percolation of liquid zinc enhance LME crack propagation [49].

2.6 LME in RSW of AHSS

When resistance spot welding zinc coated AHSS, LME is concern. Figure 2.14 show the LME crack in as-welded sample and cross-sectional view in zinc coated TRIP steel. During RSW process, the coating on the surface of the 3G-AHSS melts because the Zn has a much lower melting (419 °C) point than that of the steel substrate (~1475 °C), providing liquid zinc. As a result, stress that develops in the constrained metal during spot welding, which allows liquid zinc to come into contact with solid steel because of that developed stress. After melting, the liquid Zn can penetrate along surface grain boundaries and potentially trigger LME cracking [51,52].

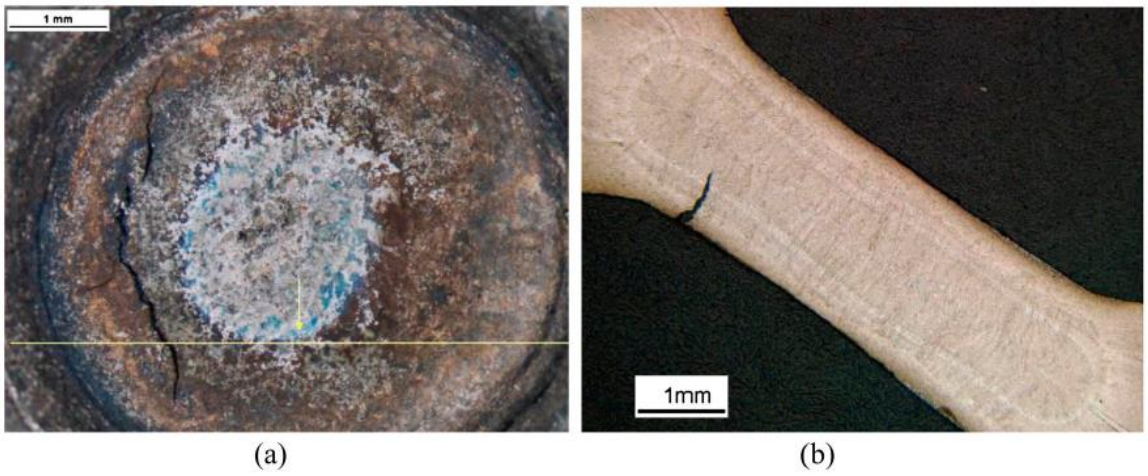


Figure 2.14: (a) As welded sample and (b) cross-sectional view of LME cracks in Zinc coated TRIP steel [53].

2.6.1 Classification of LME Cracks during RSW

LME crack severity was determined based on their position relative to the weld geometry. According to the literature [54,55], LME cracks can be categorized into three groups:

1. Cracks found at the weld indenter or center (Type A), which comes in direct contact with the electrode when welding.
2. Cracks found at the weld shoulder (Type B), which is also comes in direct contact with the electrode while welding.
3. Cracks found at the notch or sheet-sheet interface (Type C).

Figure 2.15 shows a schematic diagram of all LME cracks found in the weld.

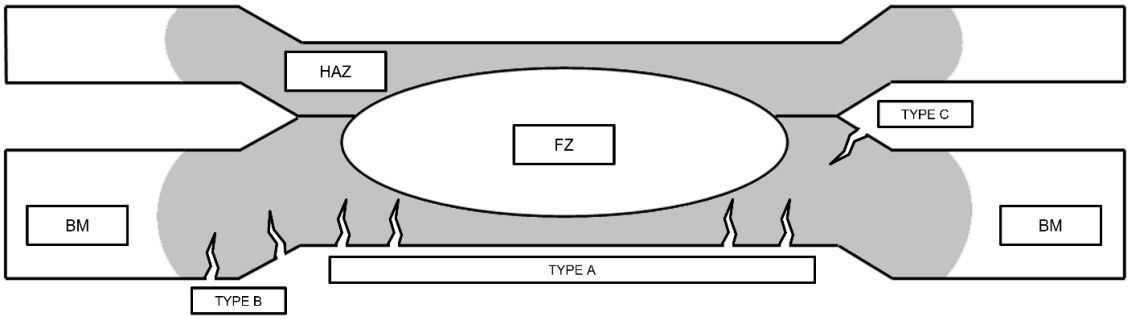


Figure 2.15: Schematic diagram showing different types of LME cracks according to the location of occurrence

2.6.2 Influence of Weld Parameters on LME

As described in section 2.3.2, to achieve the desired welding performance, several parameters can be adjusted. Heat input and diameter of weld nugget are directly influenced by welding time, welding current, and electrode force (Equation 2.1). Over the past fifteen years, a considerable amount

of research has focused on minimizing LME by adjusting welding parameters and boundary conditions during the RSW process to facilitate the incorporation of 3G-AHSS in the automotive industry. LME cracking severity is generally higher when a higher heat input is applied. As a result of a high heat input, the nugget grows and expands rapidly, causing high stress at LME-susceptible locations in the weld [22]. According to Ashiri *et al*. [44], LME cracking only occurs when the diameter of nugget exceed a critical size.

Different welding parameters have different influence on LME cracking severity. In particular, when welding time is increased, the time at elevated temperature in the RSW process is also increased. Longer welding times increase the diffusion of zinc into the grain boundaries of steel when stress is applied from the electrodes to the metal sheets [56], leading to more severe cracking. The electrode force has direct influence on LME. The lower electrode force decreases the cooling effect leading to LME. Choi *et al*. [57], concluded that the cooling stage is affected by low electrode forces, causing an increase in heat input and reduced cooling efficiency as the contact area between the electrode and workpiece is reduced. As a result of lower electrode force, the workpiece is maintained at a high temperature for a longer period of time, and Zn penetrates easily under these conditions, causing LME. The hold time also plays an important role in formation of LME crcaks. During welding, water is passed around the Cu electrodes to cool welded parts. The cooling of spot welds is controlled by the holding time. Therefore, it has been reported that increasing hold time reduces LME severity [43,53,54,58].

Aside from the effects associated with welding parameters, electrode geometry and misalignment also affects the severity of LME. Previous studies have shown that electrode geometry influences LME sensitivity and crack distribution location. DiGiovanni *et al.* [59] reported that by reducing the contact area between the electrode and the workpiece, the radius-type electrode reduces

LME cracks as compared to B-nose and truncated cone-type electrode. This reduces the temperature during hold time, which is important to reducing LME cracks. As the cooling effect increase, the duration time of liquid zinc reduces which results in a lower LME crack. An unbalanced stress field on the workpiece is caused by misaligned electrodes placement, resulting in stress concentrations which are conducive to LME crack occurrence.

2.6.3 The Influence of LME on Weld Mechanical Performance

Currently, the effect of LME on mechanical performance of resistance spot welds is unclear. Benlatreche *et al.* [60] and Choi *et al.* [57] studied the effects of LME cracks separately on the tensile shear strength, cross-tension strength and fatigue resistance spot welds. Benlatreche *et al.* observed that mechanical properties were unaffected by LME cracks. However, Choi *et al.* revealed a significant reduction in mechanical performance of the weld with LME crack length larger than 500 μm. DiGiovanni *et al.* concluded that the location of LME crack occurrence is also an important factor in determining whether the LME cracks will affect the lap shear strength. During the tensile lap shear testing, the load on weld was not uniform, and only cracks in highly stressed areas cause the reduction in weld strength [59,61]. Thus, further research needs to be conducted to understand the effect of LME on mechanical performance of the spot weld.

2.6.4 LME in Dissimilar Joint

As discussed in section 2.4, the dissimilar welding (especially thick-thin joint) used in automobile manufacturing to join BIW structure components with thin sheet (used as an automobile skin components). It is important to evaluate the LME sensitivity in dissimilar joint. Benlatreche *et al.* [62] studied LME severity of three different materials (DP1180 EG, TRIP 780 EG, 1180HF CFB EG) using two different stack-up (two sheet and three sheet). Figure 2.16 shows two different stack-up used

for LME severity evaluation. Their study concluded that among the materials evaluated for LME sensitivity, DP1180 EG is not sensitive to LME cracking. However, 1180HF EG CFB as well as TRIP 780 EG both are highly susceptible to LME.

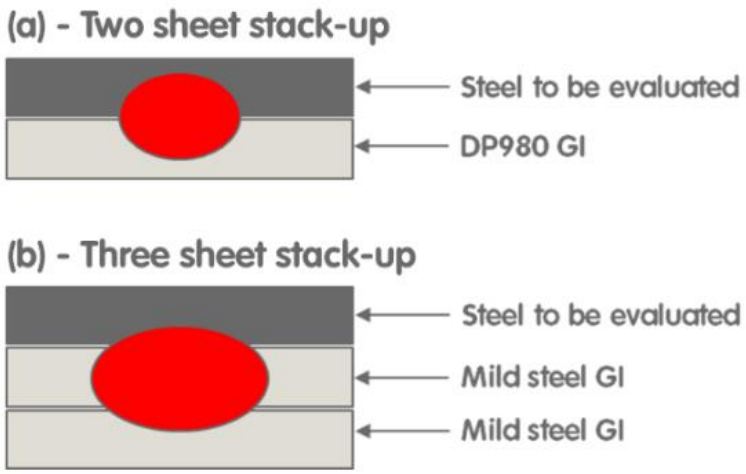


Figure 2.16: (a) Two sheet stack-up and (b) Three sheet stack-up used for LME severity evaluation [62].

Barthelmie *et al*. [63] studied LME in dissimilar joints and concluded that by using larger electrode caps and force, LME crack length was reduced to 50%. In a study by Ling *et al.* [64] using 1.4 mm thick Q&P 980, 2.0 mm thick low carbon steel (LCS), and 0.7 mm LCS dissimilar RSW joint, found that most cracks formed on the Q&P 980 side. The available literature focuses on the LME susceptibilty of different AHSS material by combining them with non-LME susceptible materials. Although this joint predominantly experiences cracking on the side of the joint with the LME susceptible material, it is very important to reduce LME cracks in this dissimilar joint since they are widely used in automobile manufacturing.

2.6.5 Methods for Suppressing LME in RSW

As discribed in section 2.6.2, the severity of LME during RSW is highly influenced by welding parameters. The severity of LME has been successfully decreased in multiple studies through the modification of welding parameters, including the use of current pulsing (attributed to a slow increase in heat generation at electrode/sheet interface) [32,61,65], varying hold time (it regulates the stress and temperature state as steel cools) [32,66], electrode force (attributed to change in cooling rate and peak temperature near the shoulder area) [41,57,67,68], and electrode geometry (attributed to change in current density and contact area, altering temperature and thermal stress around the weld pool) [59,69–71].

Previous research by Barber et al. [72] with the material used in this study found that using a 5-pulse welding schedule resulted in an 86% decrease in LME severity. In addition to this, in this study, it has been reported that LME severity decreased dramatically at very short (100 ms) and long hold durations (1000 ms), with the typical hold time of 167 ms creating the most severe LME cracks. DiGiovanni et al. [59] showed that LME suppression can also be achieved by using a radius-type electrode.

A significant amount of recent research has focused on the impact of welding process parameters on the severity of LME during RSW [73]. However, the effect of manufacturing conditions on LME cracking which often increase stress in a workpiece, has not been fully explored. In a study by Frei and Rethmeier, a welding process with external loading mimicked the effects of mechanical restraint or residual stresses to determine the impact of manufacturing conditions on LME. Their results showed that when a material is loaded to 60% of its yield strength, LME severity increases. A recent study by DiGiovanni et al. [74] showed that materials have inherent differences in terms of the amount

of pre-strain required to trigger LME cracking and concluded that low susceptibility materials are robustly manufacturable and LME resistant. However, highly sensitive materials require ideal manufacturing conditions to prevent severe LME cracking. In a study on LME by WorldAutoSteel, an external tensile stress was applied by 60% of material's yeild strength. The results showed that without any application of external tensile stress, the material does not exhibit LME. However, when material is experiencing external stress by 60% of material's YS, severe LME was observed. The application of external load during the resistance spot welding of zinc coated AHSS increases the tensile stress field to the sample and thus causing more severe LME cracks.

Angular misalignment of the electrodes is an another common industrial disturbance factor. DiGiovanni *et al*. [75] studied the influence of electrode misalignment on LME and their study concluded that as the angle of electrode misalignment increases the severity of LME increases. In addition to this, it was also concluded that misalignment of electrode causes the workpeice to bend, resulting in external mechanical stress. As welding with misaligned electrodes increased mechanical distortion, the severity of LME increased [75]. K. Pearson *et al*. [76] studied the method to reduce LME by selecting appropriate welding parameters and testing them on industrial imperfections such as electrode misalignment, welding under pre-strain, and welding with a gap. Their study concluded that despite the material having low LME severity in an ideal setup, industrially-relevant disturbance factors significantly increased LME severity. All of the welding parameter optimization studies for LME reduction has focused on similar joints.

A number of studies have focued on the LME susceptibilty of different AHSS material by combining them with low carbon steels (dissimilar joint) [62,63]. However, one aspect regarding LME reduction that has been generally neglected within the available literature is the RSW process

optimization for dissimilar joints to reduce LME cracking severity. Dissimilar welding is industrially relevant since no single available material can satisfy all requirements, and due to that, various material combinations are being used in automobile industries [77]. These joints are typically more sophisticated than similar welding due to the difference in thicknesses and resistivities between two sheets which causes variation in nugget penetration depths. More works needs to done to develop a welding schedule that reduces LME severity in a vehicle made up of dissimilar thick-thin RSW joints from AHSS and IF steel and the mechanism associate with LME supression while using developed welding schedule. In additon to this, more investigation also needs to be done to validate the robustness of that welding schedule by testing it on joints that experienced setup issues encountered during automotive assembly: electrode misalignment and sheets loaded under tension during welding as common industrial disturbance factors.

Chapter 3 Methodology

One of the primary objectives of this research is to reduce LME cracking severity dissimilar thick-thin RSW joints from 3G-980 and IF steel, by modifying welding parameters. Two different welding parameters are explored: two-pulse welding parameters similar to those defined by AWS D8.9 standard for similar joints (here-in-after referred to as baseline welding parameters) and five-pulse welding parameters for LME reduction (here-in-after referred to as optimized welding parameters). The second goal of this research is to validate the robustness of the welding schedules (both baseline and optimized) investigated in joints that experienced setup issues encountered during automotive assembly: electrode misalignment and sheets loaded under tension as common industrial disturbance factors. The materials and methods used in both of these studies are detailed in this chapter.

3.1 Materials

In this study, a 3G-980 with a nominal thickness of 1.4 mm, galvanized (GI) coated, and one GI coated interstitial free (IF) steel with a thickness of 0.6 mm were examined. Both materials used in this study were produced industrially, and coated with zinc by using hot-dip galvanizing. The steels were donated by the Auto/Steel Partnership (A/SP). The mechanical properties of 3G-980 were measured by performing standardized uniaxial tensile tests using an MTS Criterion 45 servo-electric tensile frame performed parallel to the rolling direction. The tensile tests were carried out at room temperature using tensile coupons with dimensions conforming to ASTM E8 [78]. Table 3.1 shows the chemical composition and mechanical properties of the materials used in this study. The engineering stress-strain curves are shown in Figure 3.1. The carbon equivalent (Ceq) was calculated according to the equation proposed by Yurioka et al. [79], as shown in equation 3.1.

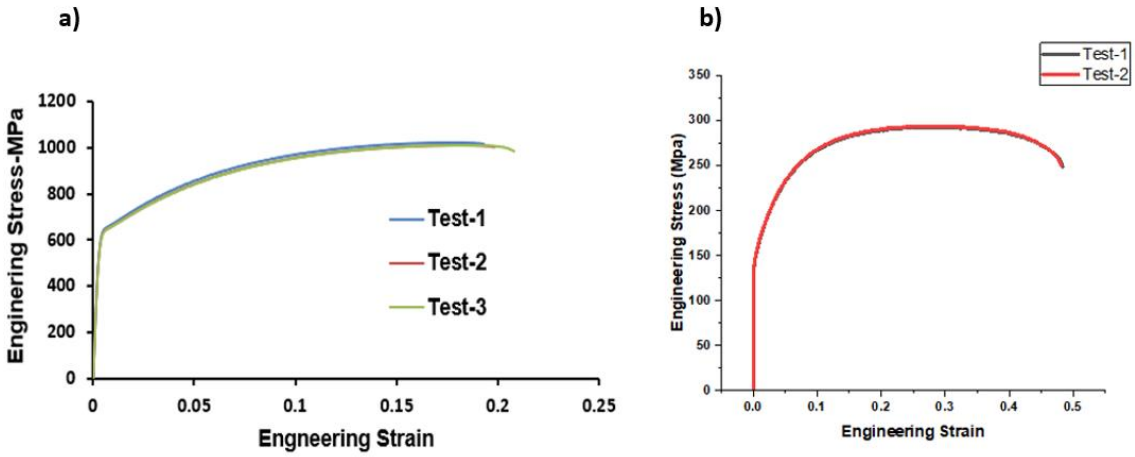


Figure 3.1: Engineering stress-strain curve for a) GI coated 3G-980 and b) IF steel materials used in this study.

Table 3.1: Test Materials chemical composition.

Material	C	Mn	P	S	Si	Cu	Ni	Cr	Mo	V	C_{eq}
3G-980	0.227	2.162	0.005	0.002	1.020	0.012	0.007	0.020	0.003	0.002	0.650
IF Steel	0.002	0.103	0.010	0.008	0.013	0.009	0.004	0.020	0.001	0.004	0.040

$$Ceq = C + A(C).\{\frac{Si}{24} + \frac{Mn}{6} + \frac{Cu}{15} + \frac{Ni}{20} + \frac{Cr+Mo+Nb+V}{5} + 5B\} \quad \textbf{(3.1)}$$

$$A(C) = 0.75 + 0.25\tanh\{20(C - 0.12)\}$$

Table 3.2: Test Materials Mechanical Properties

Material	Thickness	Yield Strength (Mpa)	Ultimate Tensile Strength (Mpa)	Elongation (%)
3G-980	1.400	634.700	1015.400	19.900
IF Steel	0.600	127.00	262.200	41.000

3.2 Resistance Spot Welding

The Resistance spot welding process was performed using an industrial 125 kVA medium-frequency direct current (MFDC) welder manipulated by a Fanuc robotic arm as shown in Figure 3.2. Force was applied with a servo-electric mechanical system capable of applying a maximum electrode force of 5.0 kN. This study used dome-radius 6R50 electrodes, having a face diameter of 6 mm and a face radius of 50 mm, with a coolant flow rate of 6 L per minute.

Table 3.2 shows three sets of RSW process parameters. As the selection of baseline welding parameters described in the Section 3.3, it is worth noting that a wide variety of process parameters, including welding current, electrode geometries, and pulsing durations combinations were examined to develop final welding conditions as outline in Table 3.2. Table 3.2 shows the parameters given by AWS D8.9 for similar joint [27] include a two-pulse welding schedule with an electrode force of 4.9 kN. This standard does not specify the welding current, as it has to be determined by the development of the weldability lobe, as shown in work by M. Shojaee *et al.* [80]. As will be explained Chapter 5, the parameters suggested by the AWS D8.9 standard for similar joint did not result in sufficient nugget penetration depth for dissimilar stack-up investigated in this study. The suggested parameters were ultimately modified (baseline parameters); accommodating at least 20% nugget penetration (the ratio of the nugget's maximum depth of fusion to the thickness pre-welded sheet thickness) [38]. Lastly, the baseline parameters were optimized for reducing LME severity (optimized parameters). The influence of the baseline and optimized parameters on LME generated during welding were then tested under the influence of two industrially relevant disturbance factors.



Figure 3.2: Resistance spot welding robot.

3.3 Selection of Baseline Welding Parameters

Images of welds made using the AWS recommended schedule revealed a lack of nugget penetration into the thinner IF steel (Figure 3.3). According to AWS D8.1 [38], nugget penetration must exceed 20% of the sheet thickness as less lower penetration depth can lead to inferior mechanical properties of the joints. Figure 3.3 shows a weld cross-section made with AWS D8.9 welding parameters, resulting in insufficient nugget penetration. Therefore, a baseline schedule was defined to attain enough nugget penetration to conform with the AWS D8.1 standard [81]. Figure 3.3 compares the percentage of nugget penetration between the AWS and baseline schedule developed in this study. As shown, the AWS schedule results in ~9% nugget penetration, whereas the baseline schedule achieves about ~35% nugget penetration.

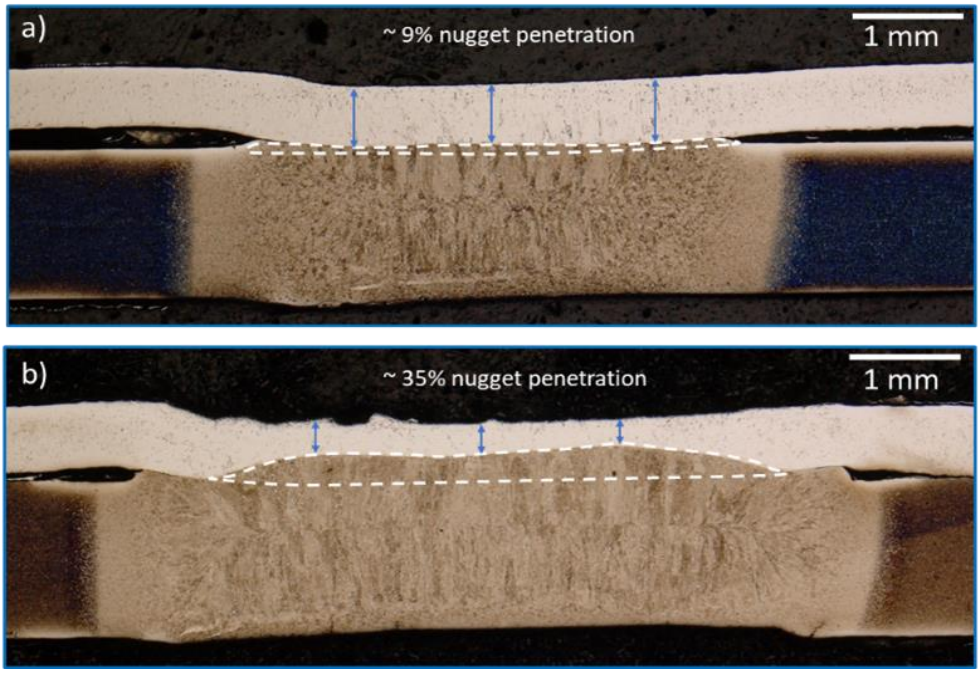


Figure 3.3: Comparison of nugget penetration between (a) AWS and (b) baseline welding schedules.

Two mechanisms are responsible for the baseline schedule producing better nugget penetration than the AWS schedule. First, the increase in penetration by incorporating lower force is related to higher heat generation at sheet-to-sheet interface. The lower electrode force increases the current density results in earlier nugget formation. Higher current density increases the resistance at sheet-to-sheet interface, resulting in higher heat generation. Secondly, shorter weld time gives less time for heat to diffuse from the weld. Additionally, it reacts more aggressively within available contact resistance, leading to preferential heating of the interface in the stack-up. This is similar to resistance spot welding of aluminum and its alloys which requires two-three times higher welding current and one third of welding time than steel because of higher thermal and electrical conductivity [82]. Decreasing both force and weld time leads to the thin/thick interface heating more readily, increasing the likelihood of

nugget penetration and attachment. As a result, the total welding time was reduced by 40% in the baseline schedule as compared to the AWS recommended schedule. These results are similar to those of work performed by Gould *et al.* [36]. In short, the baseline schedule produces heat much more rapidly compared to the AWS schedule leading to increase in nugget penetration.

Table 3.3: RSW process parameters utilized in this investigation for a dissimilar joint.

Welding schedule	Electrode Face geometry (mm)	Electrode force (kN)	Squeeze time (ms)	Pulses	Pulse length (ms)	Hold time (ms)	Cooling time between pulses (ms)	Current (kA)
AWS recommended parameters for similar joint	7 Flat	4.9	167	2	167	167	33	
Baseline	6R50	2.1	167	2	100	167*	33	9
Optimized	6R50	2.1	167	5	40	50	16	9.2

*see appendix

Table 3.4: RSW process parameters utilized in this investigation for a similar joint.

Welding schedule	Electrode Face geometry (mm)	Electrode force (kN)	Squeeze time (ms)	Pulses	Pulse length (ms)	Hold time (ms)	Cooling time between pulses (ms)	Current (kA)
Baseline	6R50	4.9	167	2	167	167	33	7.7

3.4 Welding Process Simulation

The RSW process was simulated using the axisymmetric finite element method (FEM) model to validate the experimental results reported in this work. A commercial finite element software tool Sysweld®, developed to model the RSW process, was used to simulate the thermal gradient experienced during RSW. The software's RSW tool was used to generate a mesh for the electrode, which had 3552 2D quad-tria linear elements. A newly developed AHSS (such as Q&P980) material's properties are not commonly known, and their experimental determination can be time-consuming. This study used the material characteristics simulation software JMatPro® to determine material's electrical, thermal, and mechanical properties, which was then integrated directly into ESI Sysweld® welding software. Figure 3.4 depicts the findings of the important temperature dependent characteristics for 3G-980, which demonstrate reasonable values and typical trends for AHSS.

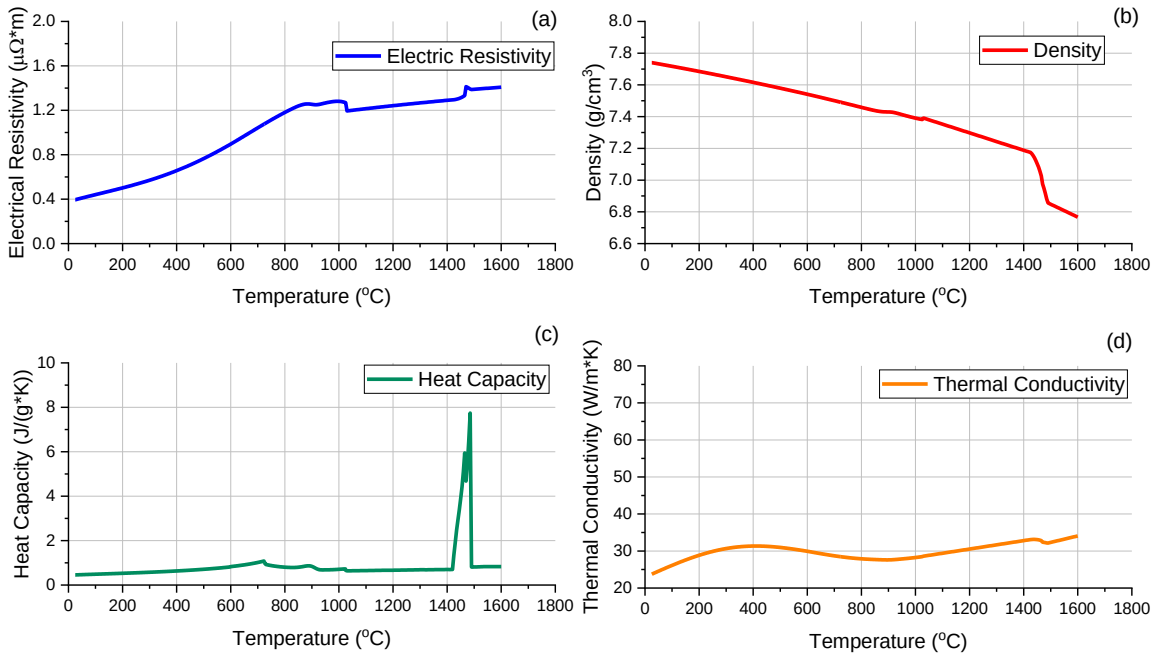


Figure 3.4: Material properties for RSW (a) Electrical resistivity, (b) density, (c) Heat capacity, and (d) Thermal conductivity

3.5 In-situ Monitering of Spot Welding Process

The RSW process was monitored using the TELOPS infrared camera (IR) M350 to validate the FEM model work results reported in this work. In this experiment, the electrodes were half-sectioned by milling them as shown in Figure 3.5. The experiments were performed by aligning two sheets (IF steel and 3G-980 steel) with the machined electrode (Figure 3.5). This experiment was conducted with the use of a fixture designed to maintain uniform sheet placement. For similar heat generation conditions as in full-section welds, electrode force and welding current were reduced to half of the values used in the full-section experiments similar to the work performed by Cho *et al.* [83]. The

IR camera was mounted on an adjustable height table to allow proper vertical and horizontal positioning.

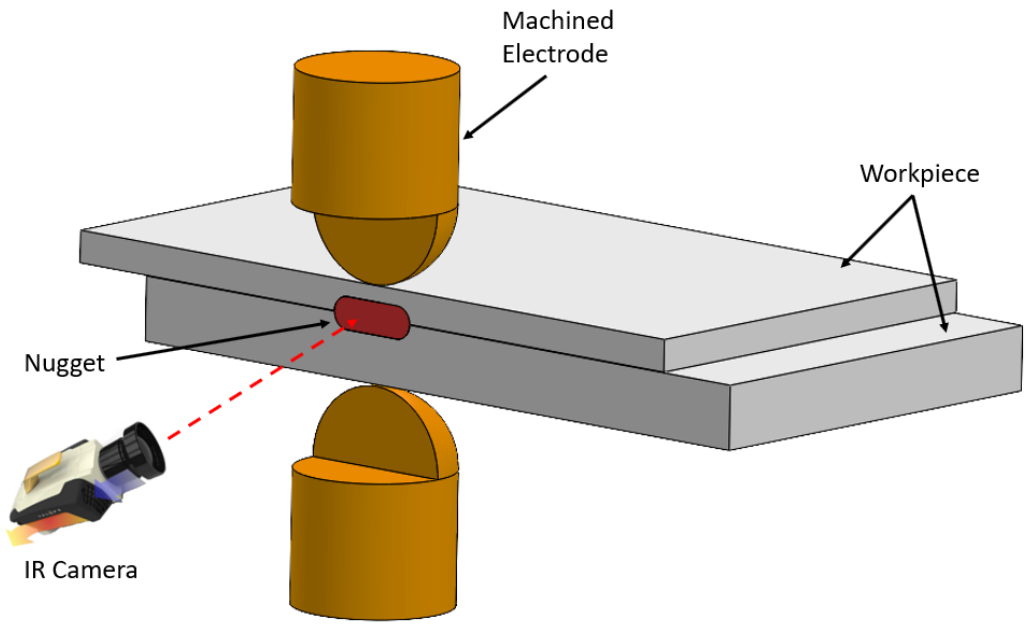


Figure 3.5: In-situ measurement of spot-welding process using IR camera

3.6 Manufacturing Variability

To verify the ability of the optimized welding schedule to mitigate LME, welds were made on joints that exhibited typical industrial disturbance factors. This study tested two sources of typical disturbance factors: welding under tension (pre-strain application) and electrode offset (electrode misalignment). The welding current in this study was selected in a way to produce a 4.5 mm nugget diameter at the sheet/sheet interface. It is worth noting that in the welds made prior to introducing industrial noise factors, the face diameter weld size (FDWS), according to AWS D8.9 [27], was maintained at 6 mm. When the industrial noise factors were applied, the welding current was not

changed since within the automotive plant operation regardless of the existence of disturbance factors the weld current is not change [10].

To assess how electrode alignment influences LME severity, welds were made using electrodes that are rotated away from their typical alignment perpendicular to the workpiece. Various electrodes misalignment values were used, they were chosen in 2° increments from 0° to 10° off-axis position. Figure 3.6 shows the schematic representation of angular electrode misalignment and coupon dimensions used for welding under tension analysis. To assess how pre-strain influences LME severity, welds were made under the influence of restraint, similar to the experiments conducted by Frei and Rethmeier [84,85]. As shown schematically in Figure 3.6, the pre-strain was applied to the 3G-980 sheet only. Pre-strain magnitude was varied between 0 (the unstrained case) and 80% of the 3G-980 sheet yield strength in 20% increments.

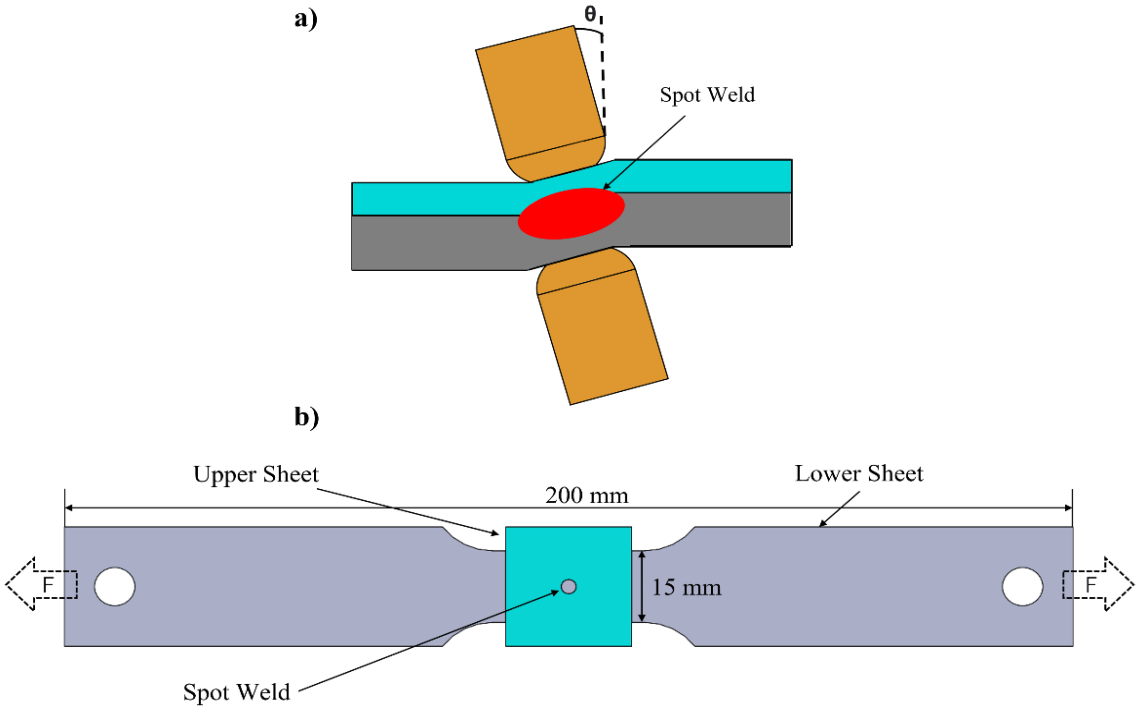


Figure 3.6: Schematic representation a) Electrode Misalignment and b) Coupon dimension used for pre-strain welding

3.7 Metallography and Microscopy

Conventional sample preparation methods were followed to observe LME cracking in the weld. Samples were cut through the plane with the most visible surface LME cracks, per the practice described by DiGiovanni *et al.* [86]. This was followed by mounting the samples in conductive epoxy resin, grinding, and polishing to a 1 μm diamond finish. LME. A 5% nital solution was used to etch the polished sample. An automated VHX-5000 optical microscope was used for microscopy. It is worth noting that all LME cracks were count in the unetched condition.

3.8 LME Severity Measurement

The cracking index (CI) equation proposed by Wintjes *et al*. [61] (Equation 1) was utilized for quantification of the LME cracking severity in each welding schedule.

$$CI = \frac{nL}{t} \tag{3.2}$$

Where n is the mean number of cracks per sample, L is the lognormal median crack length, and t is the thickness of the sheet. Crack depth was measured as the straight-line distance from the surface opening to the crack root. It is worth noting that all LME cracks were counted from the polished samples without etching. Figure 3.7 shows the measurement of LME crack from crack opening to crack tip. A cracking index is a ratio of the total length of cracks in the weld cross-section to the thickness of the sheet. In the dissimilar setup, LME cracks were only observed in the 3G-980 sheet, and as a result, cracks were only counted for that sheet.

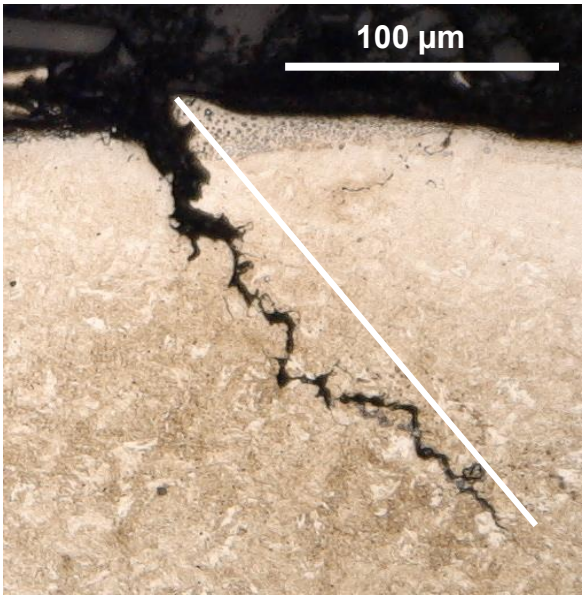


Figure 3.7: LME crack length measurement form surface opening to crack root.

For LME severity analysis, the cracking index was calculated from crack observations using five replicate welds. All error bars in cracking index graphs represent the 95% confidence interval of the measurements.

LME crack severity was determined based on their position relative to the weld geometry. According to the literature [54,55], LME cracks can be categorized into three groups: cracks located at the weld indenter or center (Type A), cracks located at the shoulder region of the weld (Type B), and the notch or sheet-to-sheet interface (Type C). Figure 3.8 shows a schematic diagram of all LME cracks found in the weld. Type A and Type B Cracks were primarily found for all the investigated conditions. For all circumstances, the severity of Type C cracking was less than a CI of 0.1; hence it was neglected.

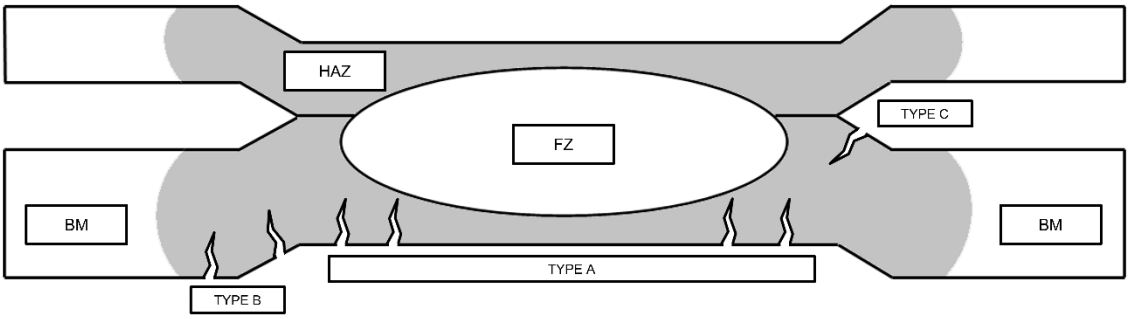


Figure 3.8: Schematic diagram showing different types of LME cracks according to the location of occurrence. (Reproduced from Figure 2.15)

Chapter 4 LME Cracking Severity in Similar and Dissimilar Joint

A majority of studies proposed different methods to reduce LME severity. These studies only focused on similar joints. Within available literature for dissimilar joints, most studies only focus on evaluating the susceptibility of different AHSS. Benlatreche *et al* [62] evaluated LME susceptibility of DP1180 and TRIP 1180 by joining them separately with mild steel. Q&P 980 was investigated by Ling *et al* [64] for LME susceptibility by combining it with low carbon steel. However, further investigation is needed for a deeper understanding of the difference of the LME response in both similar as well as dissimilar joints and methods to suppress it. In this chapter, two different types of joints have been proposed to compare the severity of LME cracking in RSW of AHSS: a similar joint (welding two sheets of 3G-980 together) and dissimilar joint (welding two different sheets; made from a 1.4 mm thick 3G-980 and a 0.6 mm thick IF steel. Both joints were welded using their respective baseline welding schedule, as described in Table 3.2 and Table 3.3 for dissimilar joints and similar joints, respectively.

4.1 Difference in Cracking Index for Similar and Dissimilar Joint

LME cracking severity results for similar and dissimilar joint shows a clear difference. LME cracking index in the dissimilar joint is higher compared to a similar joint for overall and individual types of cracks. To understand LME cracking behavior in dissimilar joints, first the difference between the dissimilar and similar joints was investigated.

Similar joints were constructed of two sheets of 3G-980, and dissimilar joints were constructed from a combination of 3G-980 and IF steel. Five welds were made for each joint type. The samples were prepared and analyzed to measure the LME cracking severity using the practice explained in

sections 3.6 and 3.7. Figure 4.1 compares the LME severity of the similar and dissimilar joints. In the case of a dissimilar joint, the LME severity is high for the total cracking index and the cracking index at each location (Type A, B, and Type C). The total cracking index for a similar and dissimilar joint is 0.78 ± 0.03 and 1.00 ± 0.04, respectively. The total CI for welds made on dissimilar sheets was increased by 30%. The increase in the CI measured from the dissimilar joint was due to an increase in both the length and frequency of cracks when compared to those from the similar joint.

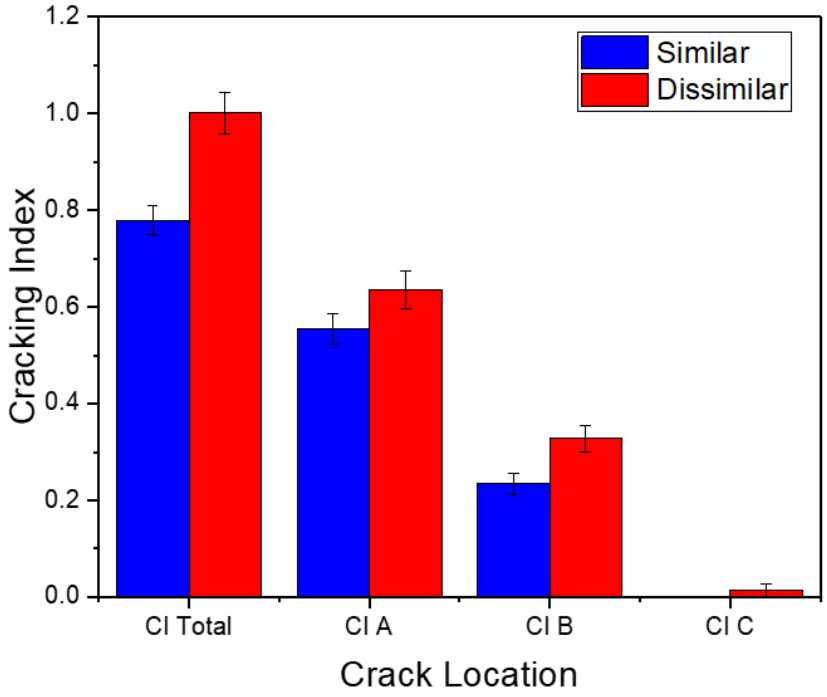


Figure 4.1: LME severity in similar vs dissimilar joint.

As seen in Figure 4.1, Type A cracks contribute more to the total cracking index for both joints than other types of LME cracks. Type A CI was 16% higher in the dissimilar joint compared to a similar joint, where mean CI increased from 0.55 ± 0.031 to 0.64 ± 0.039 for similar and dissimilar joints,

respectively. In short, it is particularly important to analyze the reasons for the increment in LME severity in a dissimilar joint.

4.2 Temperature Distribution in Similar and Dissimilar Joint

To determine the cause of LME severity increment in a dissimilar joint, welds were made and cross-sectioned. Figure 4.2 shows the result of the weld cross-section in both joints. The weld cross-section results reveal a clear difference in a distance between fusion boundary and electrode sheet interface. Since the fusion boundary is very close to the electrode/sheet (E/S) interface in the dissimilar joint, the surface near the electrode/sheet interface experiences high temperature. As described in the Section 2.5.1, the temperature is one of the factors contributing to LME, and higher temperature close to the electrode/sheet interface is one of the reasons increasing LME severity in a dissimilar joint.

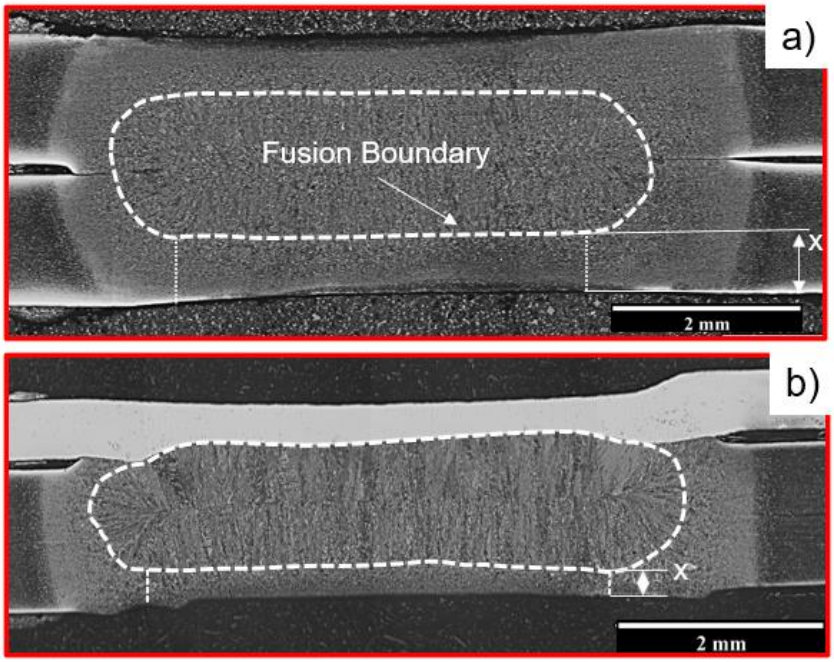


Figure 4.2: Weld cross-section showing FB for (a) similar joint and (b) dissimilar joint.

4.3 Quantification of Distance between Fusion Boundry and Electrode/Sheet Interface.

The weld cross-section visually reveals that the fusion boundary is very close to the electrode/sheet interface in a dissimilar joint. However, it is critically important to quantify the distance for both joints. Figure 4.3 shows the distance comparison between similar and dissimilar joint. As shown in Figure 4.3, the error bars in the graph represent 95% confidence intervals. As described in the graphs, the distance measurement was carried out using five weld replications for each joint type. In a similar joint, the average distance between the fusion boundary and the electrode/sheet interface is 0.697 ± 0.036 mm. However, it decreases by 62% in a dissimilar joint and is measured at an average of 0.236 ± 0.040 mm. Overall, the result from the distance quantification shows that dissimilar joints experience higher heat near the electrode sheet interface than similar joints because of the shorter distance between fusion boundary and electrode/sheet interface.

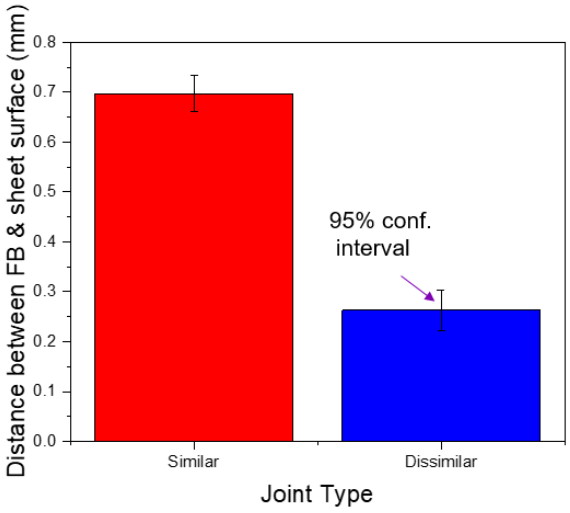


Figure 4.3: Quantification of distance between fusion boundary and electrode/sheet interface measured for five weld replicates.

4.4 FEM Analysis of Temperature Distribution for Similar and Dissimilar Joint

For a deeper understanding and to validate the result of an experimental weld-cross section, the welding process was further simulated using FEM analysis software Sysweld® using the practice described in Section 3.4. It is worth noting that the temperature scale in both simulations is above zinc melting temperature (419°C), indicating that all temperature colors in Figure 4.4 contributed to LME cracking since LME cracks occur above the zinc melting temperature. Figure 4.4 shows the FEM simulation results of temperature distribution upon current termination. The results from the FEM simulation also reveal a clear difference in the distance between the fusion boundary and the electrode/sheet surface. It shows that the fusion boundary in a dissimilar joint is very close to the electrode/sheet surface and increasing the temperature compared to a similar joint. The respective maximum surface temperature during welding cycle for a similar and dissimilar joint at weld indent area is 853°C and 978°C, respectively. This simulation result aligns with the weld cross-section for both types of joints.

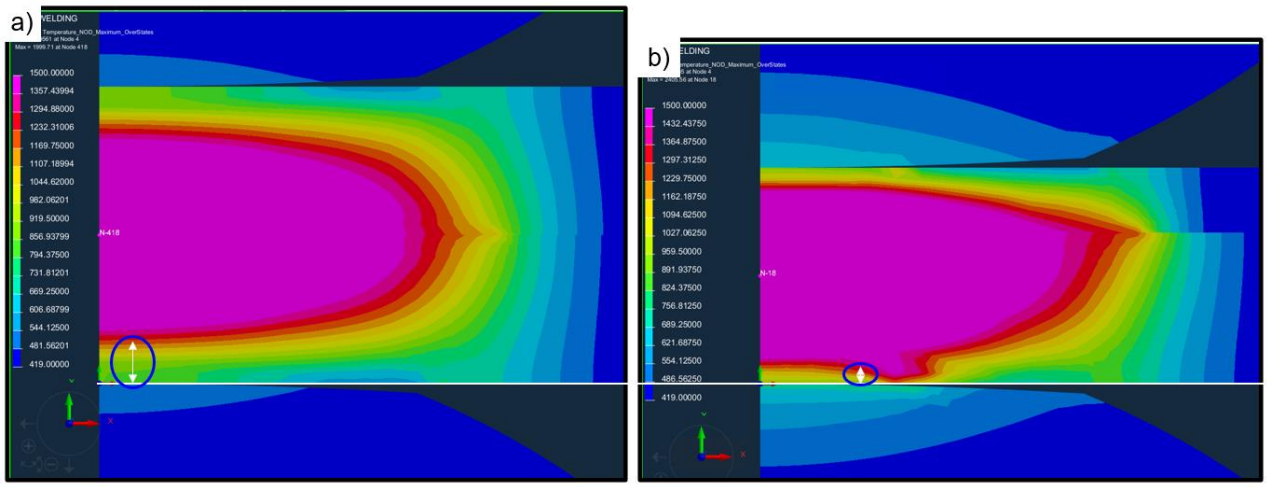


Figure 4.4: Weld Simulation showing Fusion Boundary for (a) Similar Joint and (b) Dissimilar Joint

4.5 Influence of Material Characteristics on Temperature Distribution

The location of nugget in the respective joints is due to differences in local heat generation in the joint. To understand this, the thermo-electrical properties (electrical resistivity, thermal conductivity and sheet thickness) of both materials in dissimilar joint must be understood.

As described in the Section 2.3.1, electrical resistivity plays a vital role in temperature generation during RSW. Figure 4.5 compares the electrical resistivity of 3G-980 and IF steel, obtained from the software JMatPro® using the material's chemistry. The results indicate that 3G-980 steel has higher electrical resistivity than IF steel. Higher electrical resistivity of the material results in higher heat generation during the RSW process. In the dissimilar joint examined in this study, the 3G-980 steel generates higher heat, leading to the nugget being located closer to the surface, which leads to higher

surface temperatures and temperature gradients in the dissimilar welds, resulting in greater LME severity.

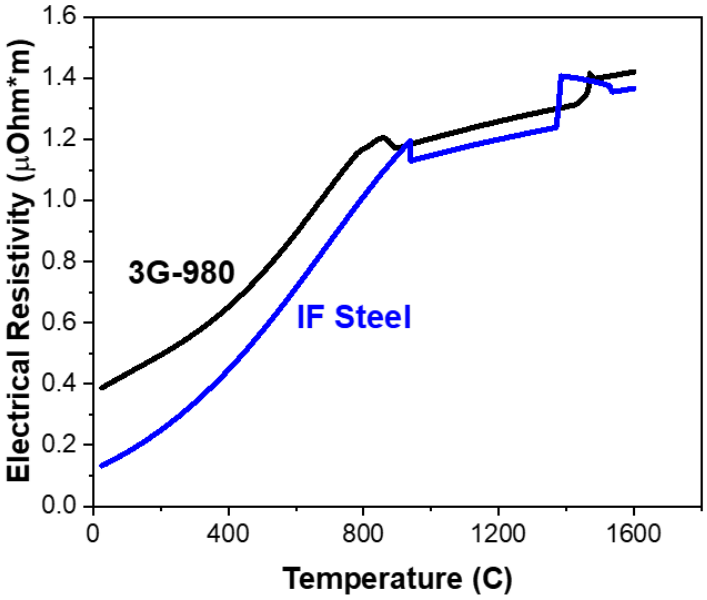


Figure 4.5: Electrical Resistivity of 3G-980 and IF steel.

In the resistance spot welding process, heat is generated by applying current. However, at the same time, heat is also conducted away from the sheets being joined to surrounding areas of the material by water-cooled electrodes. The thermal conductivity of a material affects how quickly the heat is extracted from the joint. Figure 4.6 shows the difference in thermal conductivity of the two materials investigated in this study. Thermal conductivity refers to the rate at which the heat is transferred through the material. In this instance, the lower heat conductivity of the 3G-980 restricts its cooling, allowing this side of the joint to have a higher temperature than the IF side of the joint.

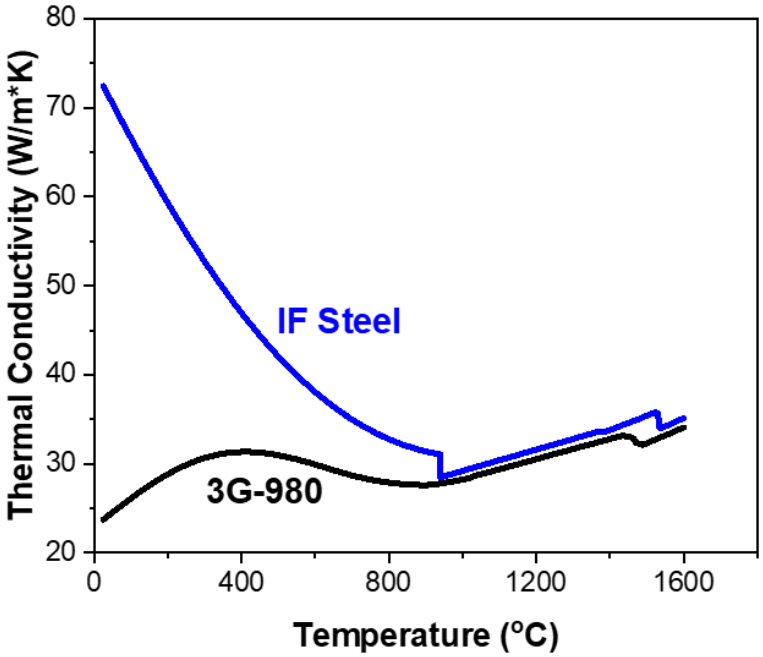


Figure 4.6: Thermal Conductivity of 3G-980 and IF Steel.

The thickness of a sheet being joined also influences temperature distribution and heat dissipation. During the resistance spot welding of dissimilar joints (thick-to-thin joint), the thin sheet dissipates more heat than the thick sheet, as the thin sheet has less volume to absorb heat. In a thick sheet, large volume of solid steel slows cooling, so the thicker material experiences high temperature for a long period of time. Also, there is a greater physical distance between the elevated temperature region and the heat sink, which increases thermal resistance. In addition to this, the thick sheet has a longer current path than that of thin sheet, leading to more heat generation and higher temperatures.

There is a linear relationship between the thickness of a sheet and material resistance. As the thickness of a sheet increases the material resistance increases. In case of thick sheet, the resistance against the flow of welding current increases which results in higher heat formation. In this

investigation, 3G-980 sheet have a higher material resistance than IF steel, increasing higher heat formation, leading to higher LME.

4.6 Simulation of Temperature Distribution throughout the Welding Process

As discussed in Section 4.5, the difference in material properties results in different temperature distributions. For further analysis, the temperature distribution at different time intervals in the welding process was carried out for both joints using the FEM analysis software Sysweld®. It is worth noting that the time intervals indicated the results from these simulations (Figure 4.7 and Figure 4.8) are with respect to the start of the first current pulse. All the temperatures in the scale bar are in ºC.

Figure 4.7 shows the temperature distribution for a similar joint at various time intervals. The simulation was carried out using a baseline welding schedule for a similar joint, as described in Table 3.3. As seen from the simulation result of a similar joint, the temperature is distributed evenly from the beginning to the end of the welding cycle. Also, the temperature started rising at the sheet/sheet interface and formed a uniform nugget as the welding process continued. In a similar joint, both sheets were 3G-980, and their material properties were identical. As a result, the symmetrical temperature distribution was observed due to symmetrical material properties.

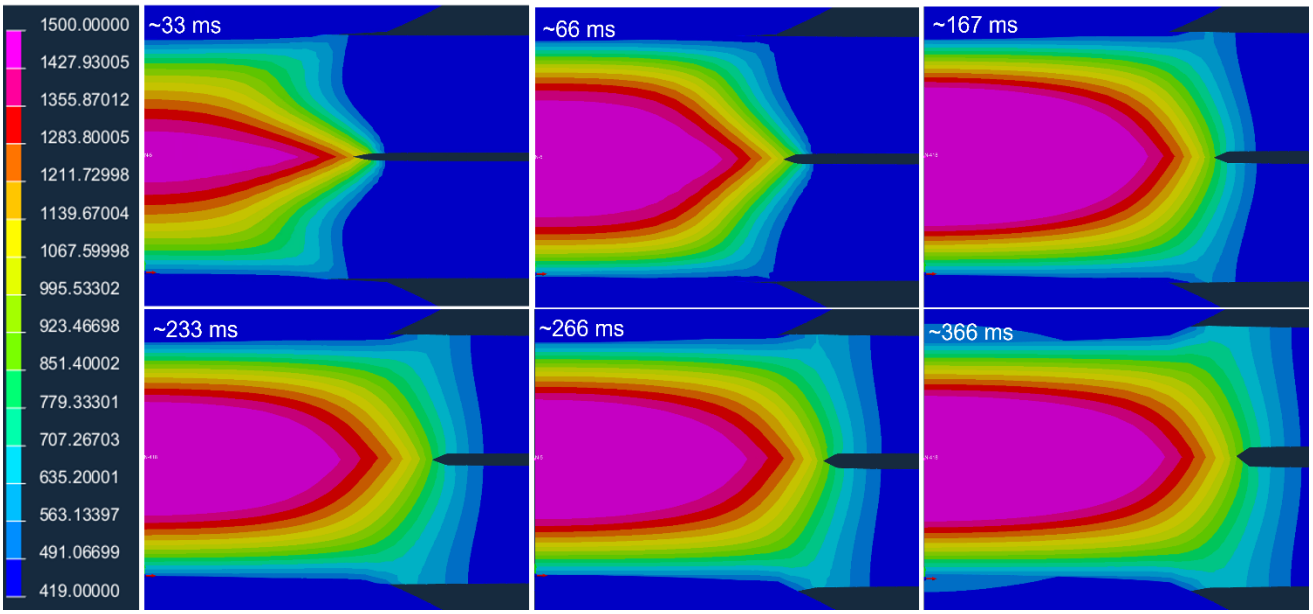


Figure 4.7: Temperature distribution in a similar joint at various time intervals.

The simulation result of temperature distribution for a dissimilar joint is shown in Figure 4.8. The results reveal that the temperature in a dissimilar joint start rising at the bottom of the 3G-980 sheet at the beginning of the first pulse. As the welding cycle progresses, the temperature rises from both sheets towards the sheet-to-sheet interface, forming a weld nugget. The difference in material properties between 3G-980 and IF steel (electrical resistivity, thermal conductivity, and sheet thickness) leads to higher heat generation in 3G-980, and greater heat dissipation in IF steel. As a result, a greater volume of the welding nugget is located on the 3G-980 sheet side of the joint. Due to this, the fusion boundary of molten nugget is very close to the electrode/sheet surface, leading to higher LME cracking in a dissimilar joint.

In short, a similar joint generates heat more uniformly, forming an equal nugget in both sheets, leading the thermal gradient away from the electrode/sheet interface. In contrast, in a dissimilar joint,

heat generation is augmented on the 3G-980 side, forming an asymmetrical nugget, resulting in higher surface temperature near the electrode/sheet interface.

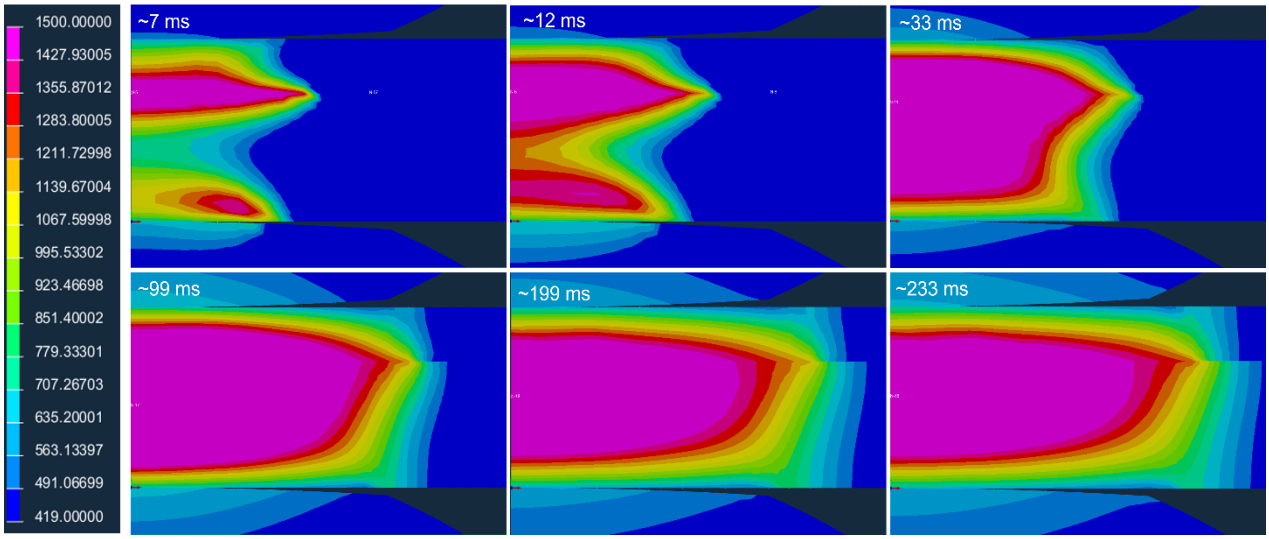


Figure 4.8: Temperature distribution in a dissimilar joint at various time intervals.

4.7 Summary

The LME cracking severity of a similar and a dissimilar joint have been examined thoroughly via experimental and simulation results. The dissimilar joint was observed to have higher LME cracking severity than the similar joint. The higher LME severity in the dissimilar joint was due to differences in temperature distribution between the two joint configurations caused by the electrical resistivity, thermal conductivity, and the thickness of the steel, which all influence temperature generation. These changes lead to differences in the location of the molten nugget in two joints. The fusion boundary was found to be closer to the electrode/sheet interface in a dissimilar joint than that of a similar joint. The distance between the fusion boundary and electrode/sheet interface in a dissimilar joint was decreased

by 62%, and the surface temperature was increased by 130°C than similar joint. The total cracking index was found to increase by 30% in a dissimilar joint.

It is very important to reduce LME cracking severity in dissimilar joints. To do this, the nugget must be shifted further from the 3G-980 sheet surface. In the following chapter, the method for LME cracking reduction will developed by adjusting resistance spot welding process parameters (optimized parameters). In addition, the LME reduction mechanism and validation of optimized welding parameters will also be explored.

Chapter 5 Mechanism of LME Exasperation and Welding Parameters Validation

The susceptibility of LME cracking was investigated using two different joint configurations (similar and dissimilar) in the previous chapter. The study provided a deeper understanding of how material properties influence LME severity in different joints configurations. In addition to this, resistance spot welding process parameters also has a large effect on LME cracking behavior. In this chapter, an industrially viable LME resistant optimized welding parameters was developed to reduce LME severity in dissimilar joint. The mechanism by which the optimized welding parameters reduces LME cracking was also explored. Finally, to check the robustness of the developed LME resistant parameters, welds were made on the joints that typically experience industrial disturbances which includes electrode misalignment and pre-strain sheets.

As described in Table 3.2, welds were made using two different welding parameters (baseline and optimized), to compared LME cracking. To understand the mechanisms responsible for LME reduction, both parameters were simulated using FEM software by practice described in Section 3.4. Following this, the results from FEM software Sysweld® were validated by using an infrared camera to monitor weld develop when using the methods described in the Section 3.5 were used.

5.1 Welding Parameters Optimization for LME Reduction

As described in the Section 2.6.2, resistance spot welding process parameters influences LME cracking severity. Therefore, a variety of welding parameters can be adjusted to influence heat generation during the welding cycle to reduce likelihood of LME cracks. In this study to lower the LME cracking severity, an industrially viable optimized welding schedule was developed by incorporating

ultra-short hold time and using a higher number of pulses. As described in Section 5.1, two mechanisms are believed to be responsible for moving the fusion boundary away from the electrode/sheet interface. First, incorporating the higher number of pulses (5-pulses) with shorter pulse lengths resulting in less heat generation near the electrode/sheet interface and providing many cooling opportunities during the welding cycle. At the same time, the baseline welding schedule had two pulses with longer pulse lengths, which resulted in higher surface temperatures. Secondly, by incorporating ultra-short hold time, electrodes are removed from the joint at an early stage, allowing heat dissipation to occur mainly in the radial direction into the sheet bulk. Lower thermal gradients between the fusion boundary and the electrode/sheet interface and slower heating and cooling rates led to radial heat transfer, resulting in lower temperature and low stress at the sheet surface. Reduced temperature gradients led to low surface stress, which resulted in reduced LME severity.

LME cracking index analysis was conducted on the baseline schedule, and a total cracking index (CI) of 1.00 ± 0.043 was calculated. The changes in the welding schedule for LME reduction (optimized welding schedule) resulted in a total CI of 0.53 ± 0.039 (46% reduction in CI compared to the baseline schedule). LME cracking index comparison between baseline and optimized welding schedule can be seen in Figure 5.1.

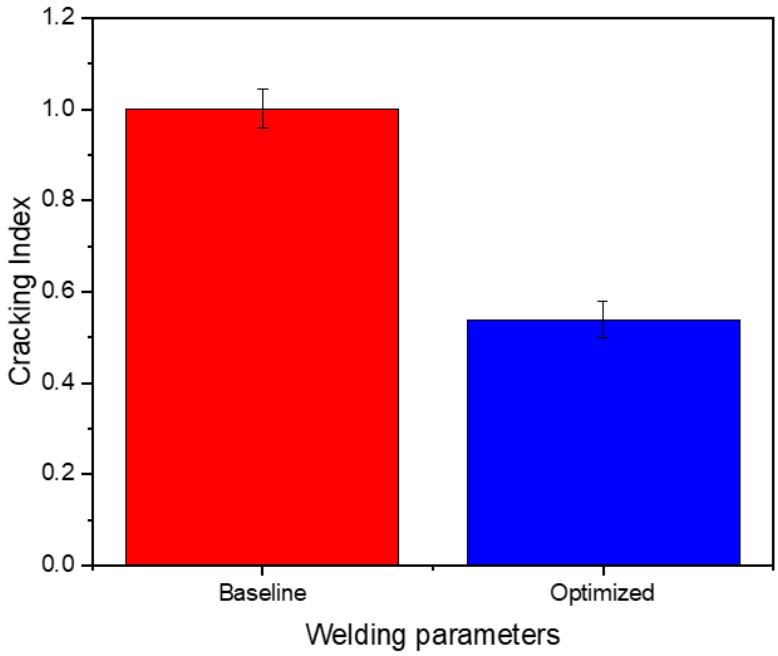


Figure 5.1: LME cracking index in baseline and optimized welding schedule.

Figure 5.2 shows the LME cracks on the cross-sectional view of both the samples welded with the baseline and optimized welding schedule. The figure includes full nugget image for both schedule and higher magnification images for cracking comparison.

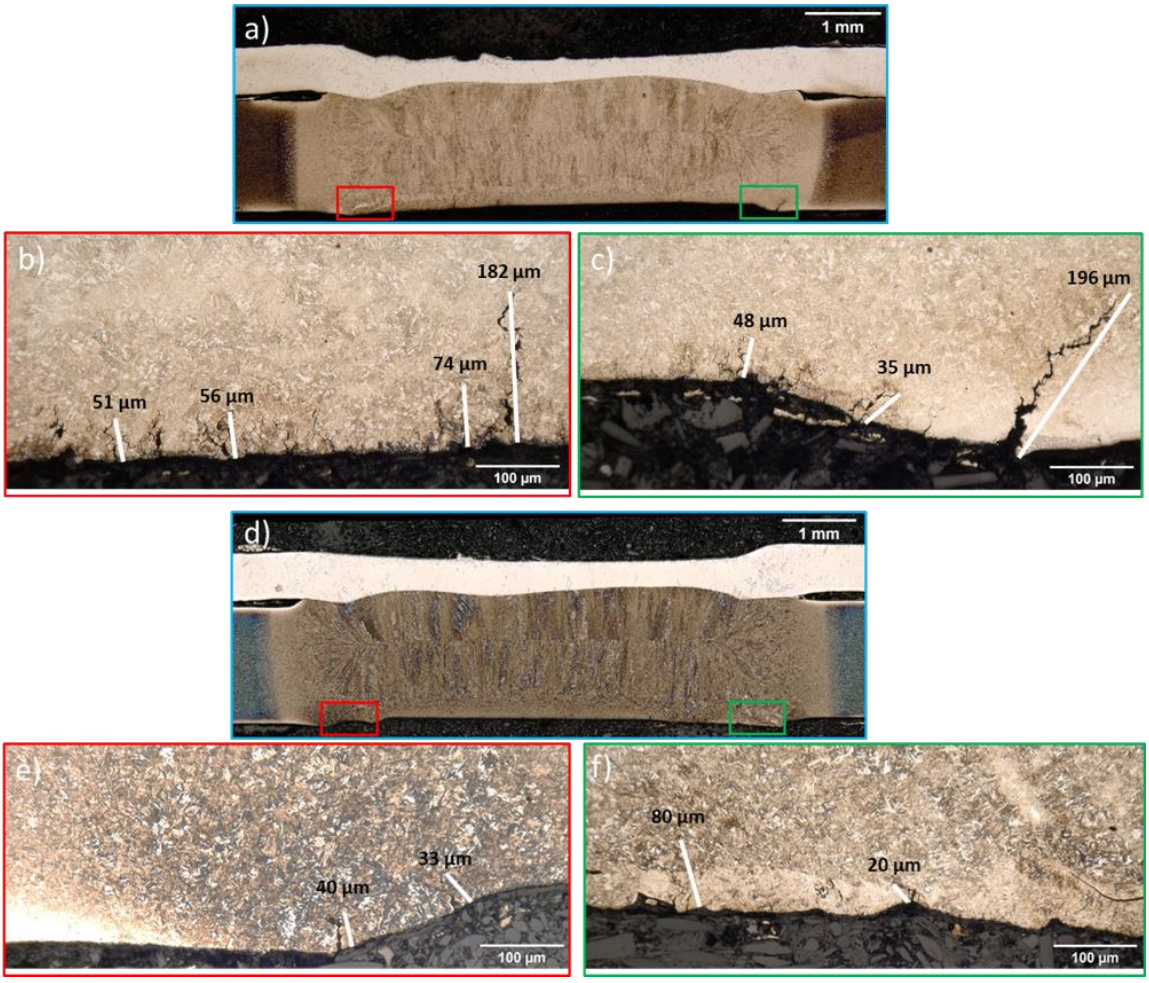


Figure 5.2: Low magnification optical images of (a) baseline and (d) optimized schedule showing spot weld cross sections. The higher magnification images illustrate LME cracks in different regions of the corresponding cross-sectional view.

5.2 Mechanism Associated with the LME Reduction

Figure 5.3 validate the fusion boundary between experimental result and simulation result for baseline and optimized welding schedule. As discussed in Section 4.2, the distance between the fusion boundary and electrode/sheet interface influences LME cracking severity. To get a more profound

understanding of the LME reduction mechanism by using an optimized welding schedule, the spot weld was cross-sectioned using the standard practice described in Section 3.7. The FEM software Sysweld® was then used to compare the experimental and simulation results. Incorporating five pulses to keep the surface cool and ultra-short hold time allowed the nugget to move away from electrode/sheet surface, resulting in the lower surface temperatures during the welding cycle. For a better understanding, the surface temperature during the welding cycle from the FEM simulation model for the weld shoulder and weld indent area of interest is shown in Figure 5.4. The graph shows that using an optimized welding schedule, both areas of interest (weld shoulder and indent area) experienced lower temperature through the welding cycle, effectively reducing LME cracking severity. The experimental and simulation results comparison shows that the fusion boundary was moved away from the electrode/sheet interface using optimized welding parameters.

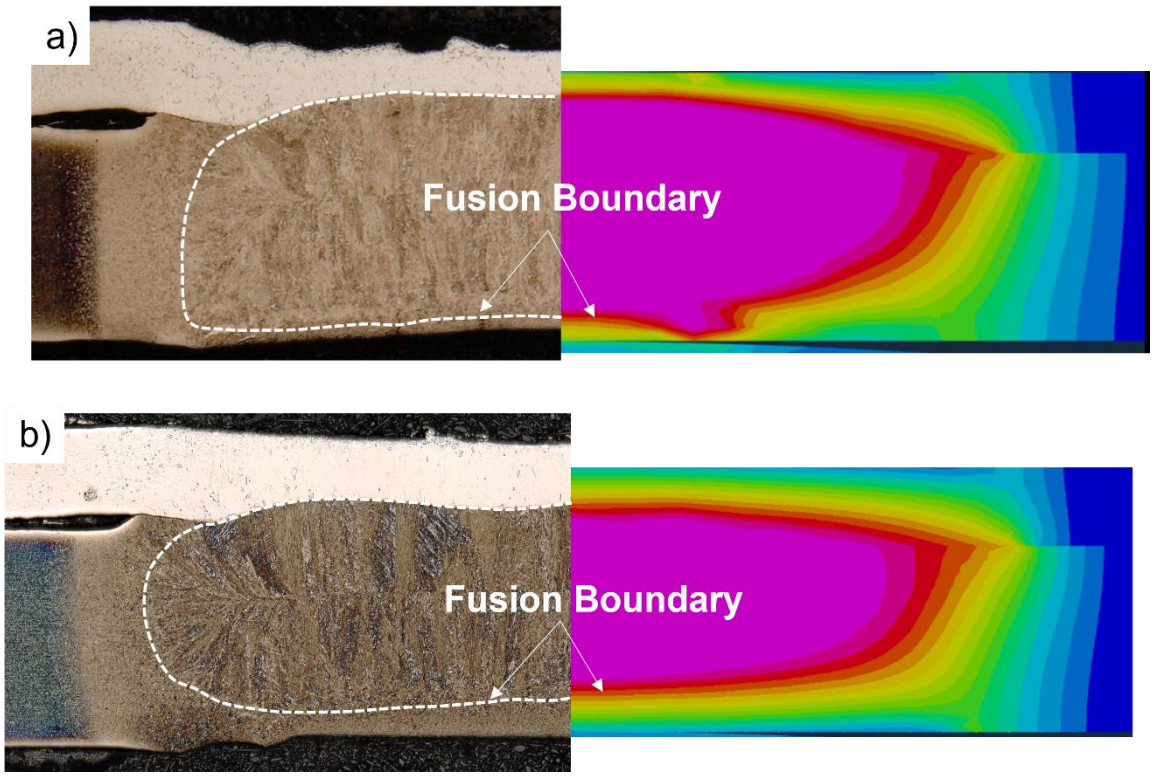


Figure 5.3: Validation of FB between experimental results and simulation results for (a) baseline welding schedule and (b) optimized welding schedule.

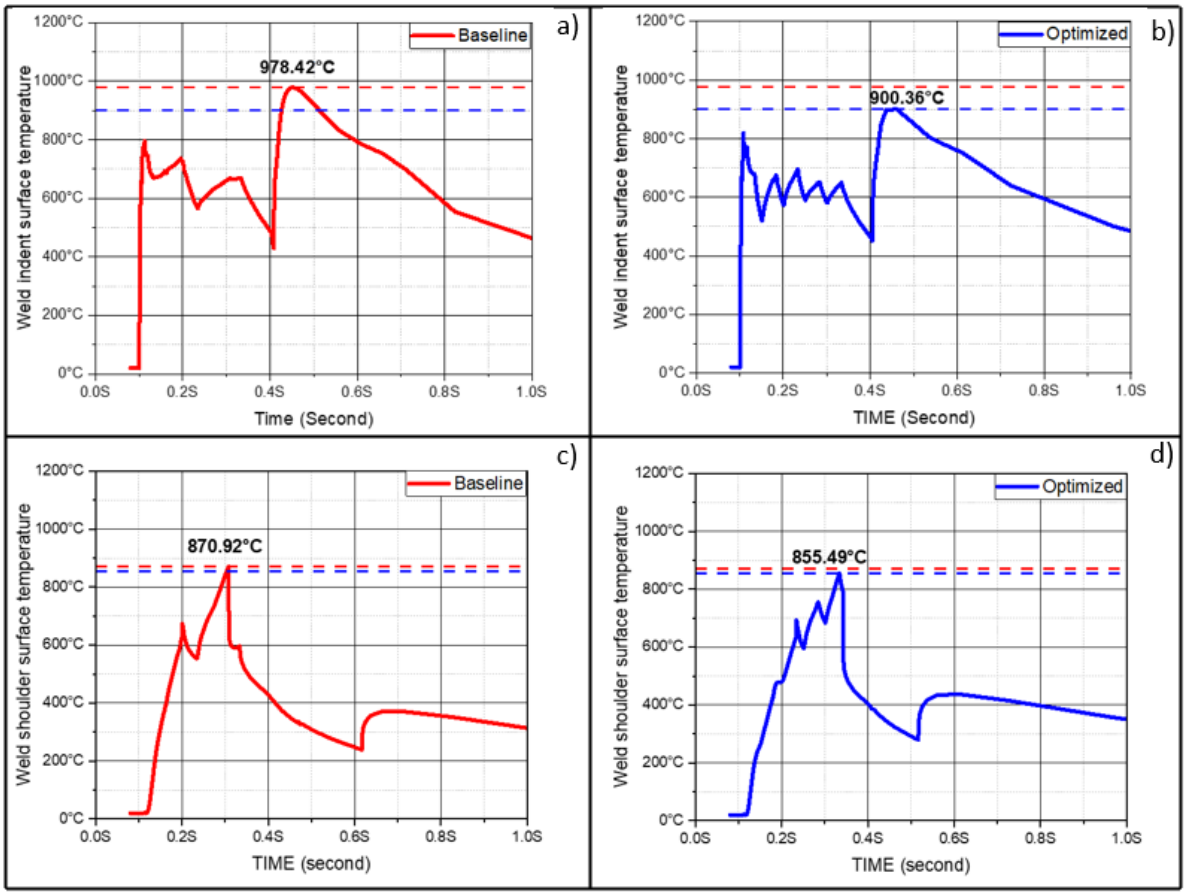


Figure 5.4: Surface temperature during welding cycle at (a) weld indent area using baseline schedule (b) weld indent area using optimized schedule (c) weld shoulder area using baseline schedule and (d) weld shoulder area using optimized schedule.

5.3 Validation of Simulation Results with IR Thermography

The experimental and simulation results showed that the fusion boundary did not extend as close to the electrode/sheet surface using an optimized welding schedule as it did using the baseline schedule. In-situ thermography was carried out to compare the fusion boundary location results from the simulation model. Figure 5.5 validates the simulation results and the results from in-situ

thermography using an IR camera. The in-situ thermography results are semi-quantitative and as shown in Figure 5.5, as the color changes from top to bottom the temperature increases. The comparison of the temperature maps of the welds made using both schedules also reveals that the weld made with a baseline welding schedule experienced higher temperatures at electrode/sheet surface (978.42°C) during the welding process than the weld made with an optimized welding schedule (900.36°C), resulting in higher LME severity.

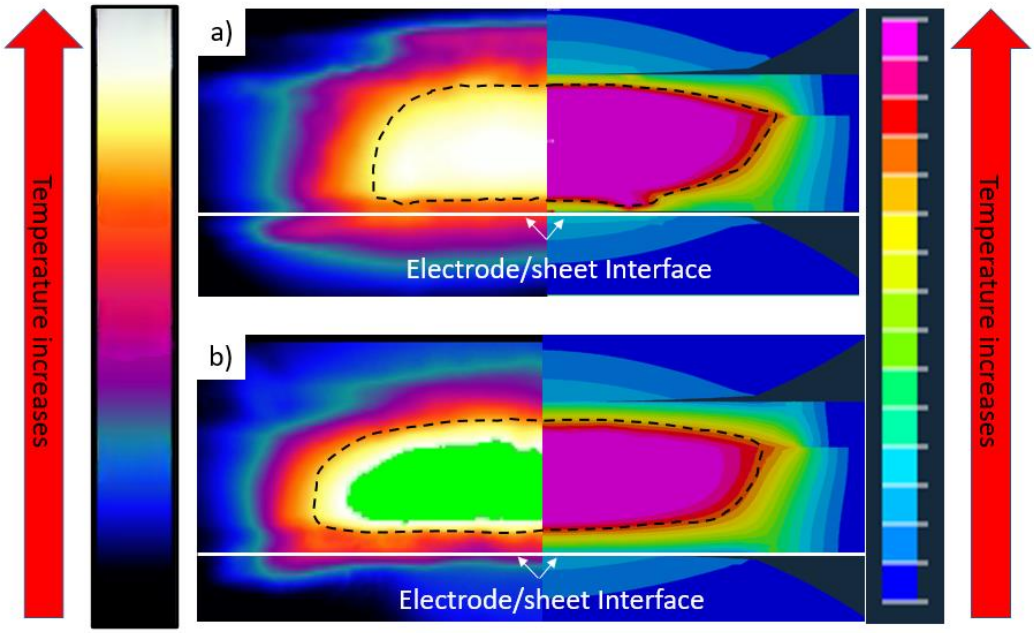


Figure 5.5: Result of fusion boundary location comparison between Sysweld® simulation and an IR camera for (a) baseline welding schedule and (b) optimized welding schedule.

5.4 Nugget Movement using the Optimized Welding Schedule

Figure 5.6 shows the distance quantification between the fusion boundary and the electrode/sheet interface. For the joint made with the baseline schedule, the distance was calculated as

0.263 ± 0.040 mm, whereas an optimized schedule showed an increase in distance by 14%, with the difference between the fusion boundary and sheet surface being 0.300 ± 0.024 mm.

The FEM simulation model along with IR-thermography and quantification results shows that the distance between fusion boundary and electrode/sheet surface using an optimized welding parameters reduces as compared to baseline welding parameters, reducing LME severity. It is important to quantify LME cracking severity to validate both (baseline and optimized) welding parameters and verify the effectiveness of these parameters using industrial disturbance factors.

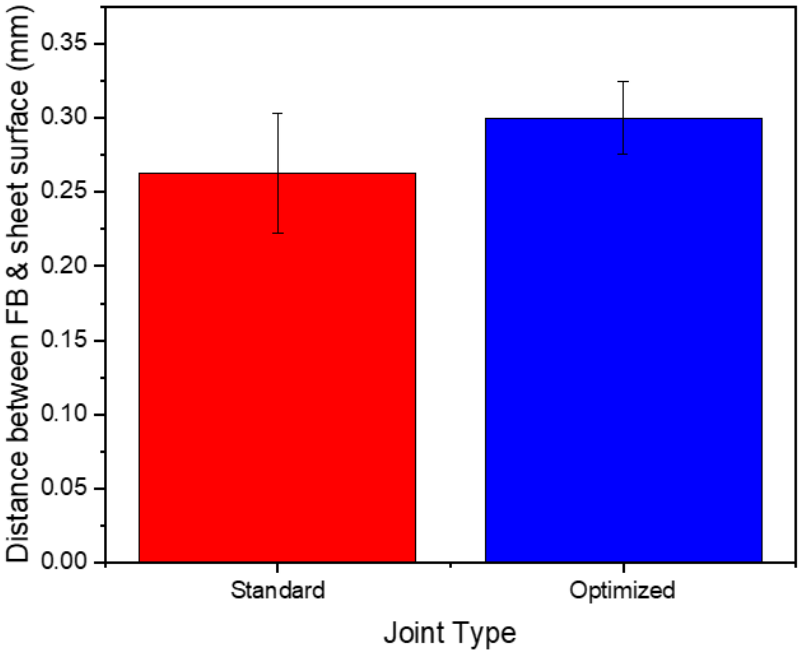


Figure 5.6: Quantification of Nugget Movement with Optimized Schedule compared to Baseline Schedule.

5.5 Validation of Welding Parameters

To validate the effectiveness of the optimized welding schedule in more realistic manufacturing situations, welds were made on joints that exhibited typical manufacturing setup imperfections. Two typical industrial disturbance factors were explored in this study: Electrode misalignment and pre-strained sheet simulates natural misalignment and residual stresses, that occur in the sheet after forming and making multiple welds, which occur during production welding.

Figure 5.7 summarizes the LME severity for welds made at different misalignment angles. Figure 5.7 (a) compares the total cracking index for the baseline and optimized schedules as a function of misalignment angle. As observed with baseline and optimized welding schedules, LME severity increased substantially with angular electrode misalignment, where mean CI increased from 1.00 ± 0.043 and 0.53 ± 0.04 at 0° to 1.15 ± 0.10 and 0.84 ± 0.06 at 10° for baseline and optimized schedules, respectively. At 10^{o} of misalignment, the baseline welding schedule showed a considerable increase in the number and length of LME cracks, with several cracks extending over 700 μm. It was seen that as misalignment increased the number of cracks that formed in welds made with the optimized schedule were shorter than those in the welds made with the baseline schedule. For the optimized welding schedule, the maximum crack length was found to be at 473 μm whereas with baseline welding schedule it was measured at 814 μm. Choi et al. [87] reported that LME cracks shorter than 500 μm would not significantly affect cross tensile strength, absorbed energy, and fatigue life of spot welds.

The total cracking index reported in Figure 5.7 (a) can be subdivided into type A, and type B LME cracking indexes, illustrated in Figures 5.7 (b) and 5.7 (c) respectively. Graphs 5.7 (b) and 5.7 (c) compare the effect of parameter optimization on the weld shoulder area and weld indent area cracking severity, respectively. As can be seen from Figure 5.7 (b), Type A cracks contribute the most to the

total cracking index compared to Type B cracks. Type A cracking index, for baseline welding schedule, increases from 0.63±0.04 at 0º of misalignment to 0.93±0.12 at 10º of electrode misalignment. The optimized welding parameters led to reduction in Type A LME severity by 38% in highest electrode misalignment (10º). The total CI for welds made with the optimized schedule was reduced by 46% prior to the introduction of joint imperfection (at 0° of electrode misalignment), demonstrating the effectiveness of the proposed optimized schedule in reducing the LME. Similarly, when electrodes were misaligned by 10°, the optimized parameters resulted in less severe cracking than measured in welds made using the baseline parameters, decreasing LME severity by 27% compared to the baseline weld schedule.

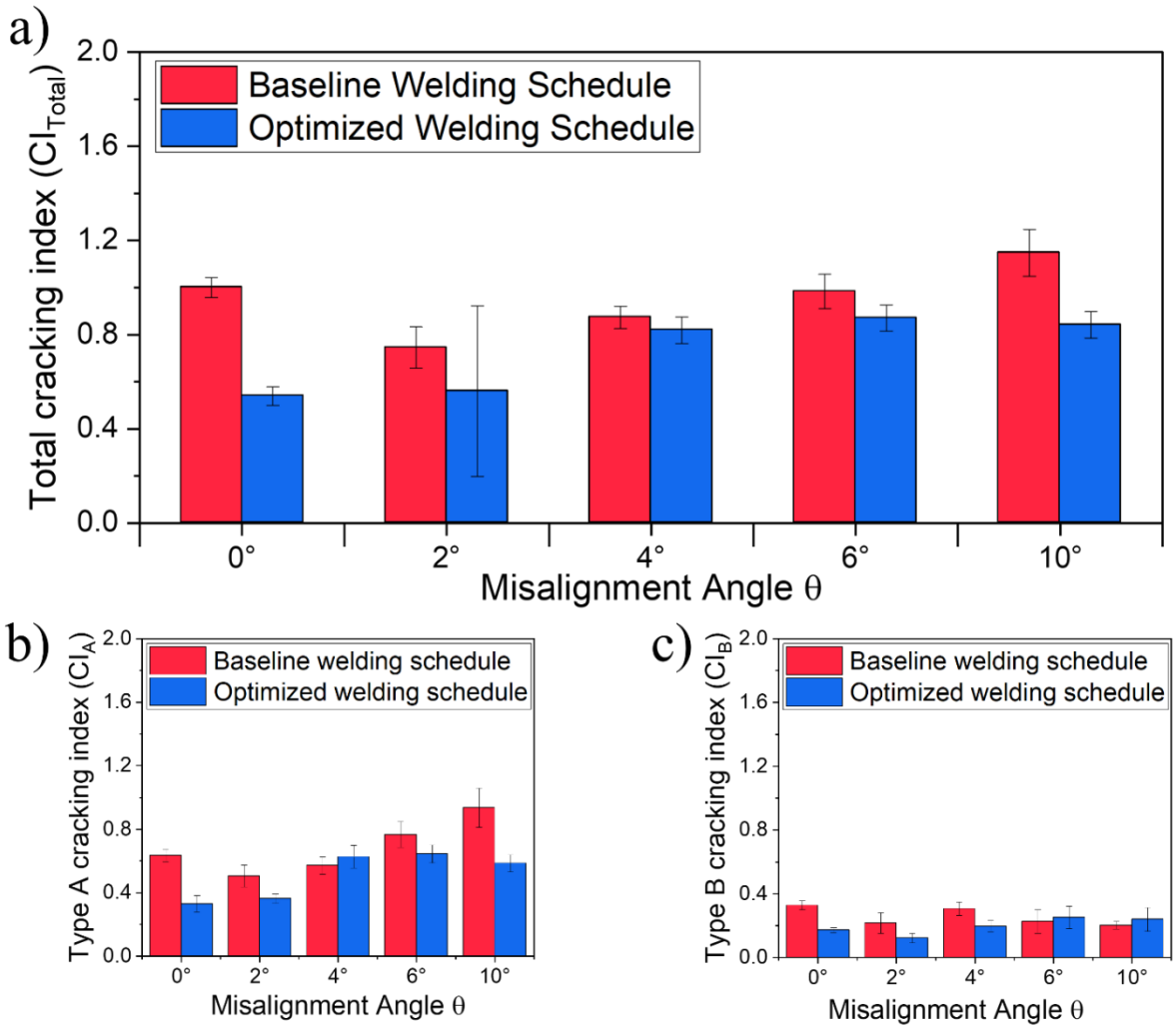


Figure 5.7: Comparison of (a) Total Cl, (b) Type A CI, and (c) Type B CI resulting from welds made with electrode misalignment for both the standard and optimized weld schedules.

To investigate the effect of pre-strain on LME severity, welds were made under specific amounts of restraints. Figure 5.8 (a) shows the total cracking index for the baseline and optimized schedule with increasing tensile loads. The results indicate that crack severity increases as the amount of pre-strain during welding increases. With increased tensile loads, the total cracking index increases

for both baseline and optimized schedules, respectively, from 0.21 ± 0.03 and 0.16 ± 0.03 in non-loaded conditions to 1.50 ± 0.09 and 0.88 ± 0.13 at 80% YS of 3G-980 sheet (507 MPa). It should be noted that the unstrained LME severity was lower than in the previous test on misalignment (Figure 5.7). It is suspected that this was due to sample geometry. The coupons used for the pre-strain tests had a lower width than those used for the misalignment tests. It was speculated that the difference in LME severity is due to difference in restrain stress. The influence of coupon geometry on LME response during RSW process is out the scope of the current study and will be further pursued in future.

Figure 5.8 shows the progression of LME severity as tensile stress increased from 0 to 80%. Figure 5.8 (b) shows that a slight increase in Type A cracks contributed to an overall increase in LME severity for the baseline weld schedule. As observed, Type A CI increased with increasing tensile load, from 0.14 ± 0.03 and 0.06 ± 0.04 under non-loading conditions (0% of pre-strain) to 0.81 ± 0.09 and 0.48 ± 0.10 at the pre-stain of 80% YS of 3G-980 sheet for baseline and optimized schedules, respectively. The optimized weld schedule mitigated LME cracking by 41% for both Type A LME cracking and total CI in weld performed under external load of 80%

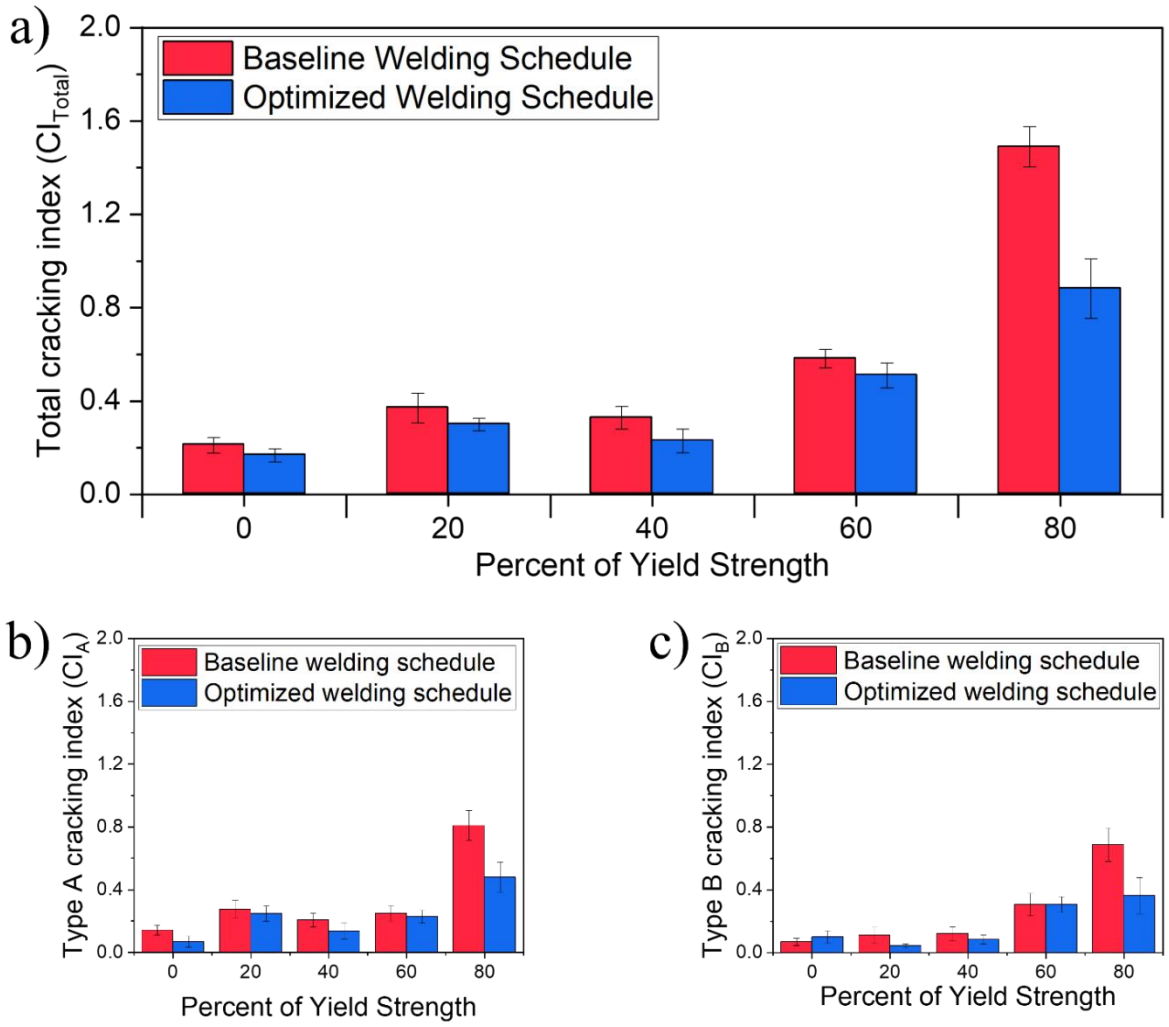


Figure 5.8: Comparison of (a) Total Cl, (b) Type A CI, and (c) Type B CI for welds made on a sheet loaded under tension using both the standard and optimized weld schedules.

5.6 Summary

Based on the result presented in this chapter, it can be seen that a dissimilar joint is generally highly susceptible to LME cracking compared to a similar joint. The material properties are critically important in temperature generation. The difference in temperature distribution throughout the welding

process resulted in different LME responses. For the baseline welding schedule, it was found that the fusion boundary was close to the electrode/sheet interface making the surface hot during the welding process resulting in higher LME severity. An optimized welding schedule includes five pulses with 40 ms of pulse length and ultra-short hold time of 50 ms, providing many cooling opportunities and keeping the surface cool during welding compared to the baseline welding schedule reducing LME severity by 46%. LME cracking severity increases as the severity of industrial disturbance factors increases. For severe electrode misalignment (10°), optimized welding schedule reduced LME severity by 27%. Similarly, for severe pre-strain application (80%), total LME severity decreased by 41% using optimized welding schedule.

Chapter 6 Conclusions and Future Work

6.1 Conclusions

This study investigated two common types of joints (similar and dissimilar) to quantify the difference in LME severity between those joints. This work explained that the high LME severity observed in dissimilar joints was due to the decreased distance between the molten nugget and the surface of the 3G-980 steel sheet. Decreased distance increased both the temperature and the temperature gradient at the sheet surface, increased the susceptibility to LME. Furthermore, welding parameters were developed to shift the nugget away from the sheet surface decreasing LME severity.

The reason that the nugget in the dissimilar welds extended closer to the electrode/sheet interface than in the similar welds was due to differences in material properties, including electrical resistivity, thermal conductivity, and sheet thickness of the 3G-980 steel and the IF steel that was used for one side of the dissimilar joint. The different material properties resulted in a difference in heat absorption in the 3G-980 sheet, which decreased the distance between the fusion boundary and electrode/sheet interface by 62% in dissimilar joints as compared to similar joints. Additionally, the results from finite element modeling software Sysweld® also showed higher temperature development close to the electrode/sheet interface, keeping the surface hot throughout the welding process.

By selecting appropriate welding parameters, the severity of LME can be reduced significantly. In this research, welding with an increased number of current pulses and ultra-short hold time (five pulses of 40 ms pulse length and 50 ms hold time) compared to baseline welding schedule (two pulses of 100 ms pulse length and 167 ms hold time) under laboratory conditions and without industrial disturbances led to a 46% reduction in LME cracking severity. More pulses with shorter pulse lengths

resulted in lower LME severity by generating less heat at the sheet surface and providing prolonged cooling time during the welding cycle. The optimized parameters increased the distance between the fusion boundary and electrode/sheet interface by 14%, decreasing LME cracking by 46%. The results from in-situ thermography and FEM software Sysweld® using an optimized welding schedule showed that the electrode/sheet interface experienced lesser temperature generation and thus reduced LME significantly.

Understanding how LME responds to manufacturing variability is essential. Although low LME severity materials may exhibit minimal cracking levels on ideal joints, crack severity increases during assembly when joints are made under non-ideal weld conditions and set-ups. Examples of industrial disturbance factors include RSW electrode misalignment and sheet pre-strain. With optimized welding schedules, the LME severity decreases, alleviating the problems encountered with the non-ideal joint condition. Although the ideal setup had low LME severity, industrial disturbance factors, including electrode misalignment and tensile loading, significantly increased the LME severity. For baseline conditions, in the case of electrode misalignment, the most severe misaligned (10°) set-up increased LME by 13%. As for pre-strain application, an 86% increase in LME severity was observed when applying a pre-strain of 80%. The increase in LME severity by increase in misalignment and pre-strain using baseline welding schedule is more severe than the optimized welding schedule.

Changing the welding parameters to reduce LME is an industrially viable technique. Compared to a baseline welding schedule using an optimized welding schedule in extreme industrially relevant disruption cases reduced LME by almost 40%.

6.2 Future Work

This work has shown that combining multiple pulses with a shorter pulse length and ultra-short hold time reduces the LME cracking in a dissimilar joint. This study has shown an in-depth analysis of the effect of different thicknesses that are being joined using material properties. Sheet thickness is an important characteristic influencing the LME cracking severity. Various sheet thickness combinations are used during automobile manufacturing depending on the application.

Further analysis is needed to determine the severity of LME by using different sheet thicknesses of IF steel while keeping a constant thickness of the 3G-980 sheet and the same nugget diameter for direct comparison. In addition, more testing must be carried out to understand the impact of LME cracking on the mechanical performance of the welded joint. In the future, an industrially viable welding schedule should be determined to decrease LME in different sheet thickness combinations by testing them on industrially relevant disturbances.

References

[1] Health and Safety Executives, “The Flixborough Disaster: Report of the Court of Inquiry”, HMSO, ISBN 0113610750, 1975. n.d.

[2] Beal C, Kleber X, Fabrègue D, Mohamed B. Embrittlement of a zinc coated high manganese TWIP steel. Mater Sci Eng A 2012;543:76–83. https://doi.org/10.1016/j.msea.2012.02.049.

[3] Kamdar MH. Review Liquid Metal Embrittlement. Treatise Mater Sci Technol 1983;25:361–459. https://doi.org/10.1016/b978-0-12-341825-8.50015-5.

[4] McNutt M. Climate change impacts. Science (80) 2013;341:435. https://doi.org/10.1126/science.1243256.

[5] Creutzig F, Jochem P, Edelenbosch OY. Transport: A roadblock to climate change mitigation. Science (80-) 2015;350:911–2. https://doi.org/10.1126/science.aac8033.

[6] Tamarelli CM. The evolving use of advanced high-strength steels for automotive applications. Steel Mark Dev Institute, Michigan 2011.

[7] Abadi MMH, Pouranvari M. Failure-mode transition in resistance spot welded DP780 advanced high-strength steel: Effect of loading conditions. Mater Tehnol 2014;48:67–71.

[8] Keith DR, Houston S, Naumov S. Vehicle fleet turnover and the future of fuel economy. Environ Res Lett 2019;14. https://doi.org/10.1088/1748-9326/aaf4d2.

[9] Keeler S, Kimchi M, Mooney PJ. Advanced High-Strength Steels Guidelines Version 6.0. WorldAutoSteel 2017:314.

[10] Pouranvari M, Marashi SPH. Critical review of automotive steels spot welding: Process, structure and properties. Sci Technol Weld Join 2013;18:361–403. https://doi.org/10.1179/1362171813Y.0000000120.

[11] Wang L, Speer JG. Quenching and Partitioning Steel Heat Treatment. Metallogr Microstruct Anal 2013;2:268–81. https://doi.org/10.1007/s13632-013-0082-8.

[12] Tan X, Ponge D, Lu W, Xu Y, Yang X, Rao X, et al. Carbon and strain partitioning in a quenched and partitioned steel containing ferrite. Acta Mater 2019;165:561–76. https://doi.org/10.1016/j.actamat.2018.12.019.

[13] Edmonds D V., He K, Rizzo FC, De Cooman BC, Matlock DK, Speer JG. Quenching and partitioning martensite-A novel steel heat treatment. Mater Sci Eng A 2006;438–440:25–34. https://doi.org/10.1016/j.msea.2006.02.133.

[14] Steel IPD, Sugimoto K, Kobayashi M, Hashimoto S. Ductility and Strain-Induced Transformation in a High-Strength Transformation-. Metall Mater Trans A 1992;23:3085–91.

[15] Wang L, Speer JG. Quenching and Partitioning Steel Heat Treatment. Metallogr Microstruct Anal 2013;2:268–81. https://doi.org/10.1007/s13632-013-0082-8.

[16] Marder AR. The Metallurgy of zinc-cozted Steel. Prog Mater Sci 1912;89:315–6. https://doi.org/10.1038/089315a0.

[17] Warnecke W, Bode R, Kothe R, Meyer L. Modern Hot Dip Coated Sheet Steel--Processing, Coating Characteristics and Fabricating Properties. Zinc-Based Steel Coat Syst Metall Perform 1990:3–17.

[18] Marder AR. Microstructural Characterization of Zinc Coatings, in: G. Krauss, D.K. Matlock (Eds.), Zinc-Based Steel Coat. Syst. Metall. Perform. Miner Met Mater Soc Warrendale 1990:55–82.

[19] Williams NT, Parker JD. Review of resistance spot welding of steel sheets: Part 1 - Modelling and control of weld nugget formation. Int Mater Rev 2004;49:45–75. https://doi.org/10.1179/095066004225010523.

[20] Mallick PK. Joining for lightweight vehicles. Mater Des Manuf Light Veh 2021:321–71. https://doi.org/10.1016/B978-0-12-818712-8.00008-2.

[21] Luo Y, Liu J, Xu H, Xiong C, Liu L. Regression modeling and process analysis of resistance spot welding on galvanized steel sheet. Mater Des 2009;30:2547–55. https://doi.org/10.1016/j.matdes.2008.09.031.

[22] Wintjes E. A Statistical Approach to Quantifying Impact of Multiple Pulse Resistance Spot Welding Schedules on Liquid Metal Embrittlement Cracking by. University of Waterloo, 2019.

[23] Zhang H. Resistance Welding: Fundamentals and Applications, Second Edition (2nd ed.). CRC Press; 2011. https://doi.org/https://doi.org/10.1201/b11752.

[24] Kimchi M. Resistance Spot Welding Fundamentas and application for the automotive industry. Morgan & Claypool Publishers; 1975. https://doi.org/10.2200/S00792ED1V01Y201707MEC005.

[25] Bhadeshia H. Microstructure and Properties. 4th ed. Elsevier. 2017.

[26] Dickinson DW, Franklin JE, Stanya A. Characterization of Spot Welding Behavior By Dynamic Electrical Parameter Monitoring. Weld J (Miami, Fla) 1980;59.

[27] American Welding Society. Test Methods for Evaluating the Resistance Spot Welding Behavior of Automotive Sheet Steel (AWS D8.9M:2012). 2012.

[28] Marashi P, Pouranvari M, Sanaee SMH, Abedi A, Abootalebi SH, Goodarzi M. Relationship between failure behaviour and weld fusion zone attributes of austenitic stainless steel resistance spot welds. Mater Sci Technol 2008;24:1506–12. https://doi.org/10.1179/174328408X262418.

[29] Mallick PK. Materials, design and manufacturing for lightweight vehicles. 2010. https://doi.org/10.1533/9781845697822.

[30] Zhang H, Senkara J. Electrothermal Processes of Welding. Resist Weld 2020:74–121. https://doi.org/10.1201/b11752-5.

[31] Hwang IS, Kang MJ, Kim DC. Expulsion reduction in resistance spot welding by controlling of welding current waveform. Procedia Eng 2011;10:2775–81. https://doi.org/10.1016/j.proeng.2011.04.461.

[32] Ashiri R, Shamanian M, Salimijazi HR. Liquid metal embrittlement-free welds of Zn-coated twinning induced plasticity steels. Scr Mater 2016;114:41–7. https://doi.org/10.1016/j.scriptamat.2015.11.027.

[33] Scotchmer N. Widening the Welding Lobe of Advanced High Strength Steels in the Resistance Spot Welding Process. Huys Ind Ltd n.d.:1–11.

[34] Autobody/Steel Partnership: AHSS Joining - Resistance Spot Weld Schedules for AHSS 2007.

[35] Chabok A, van der Aa E, Basu I, De Hosson J, Pei Y. Effect of pulse scheme on the microstructural evolution, residual stress state and mechanical performance of resistance spot welded DP1000-GI steel. Sci Technol Weld Join 2018;23:649–58. https://doi.org/10.1080/13621718.2018.1452875.

[36] Gould J, Peterson W, Cruz J. An examination of electric servo-guns for the resistance spot welding of complex stack-ups. Weld World 2013;57:243–56. https://doi.org/10.1007/s40194-012-0019-x.

[37] Shen J, Zhang Y, Lai X, Wang PC. Modeling of resistance spot welding of multiple stacks of steel sheets. Mater Des 2011;32:550–60. https://doi.org/10.1016/j.matdes.2010.08.023.

[38] American Welding Society. AWS D8.1M, 3rd Edition, 2021 - Specification for Automotive Weld Quality Resistance Spot Welding of Steel, ISBN:978-1-64322-178-6 2021.

[39] Aliya D, Becker WT, Shipley R. ASM Handbook Volume 11: Failure Analysis and Prevention. ASM Int 2018:1061–77. https://doi.org/10.31399/asm.hb.v11.a0005695.

[40] Vermeersch M, De Waele W, Van Caenegem N. LME susceptibility of galvanised welded structures of high strength steels. Int J Sustain Constr Des 2011;2:442–7. https://doi.org/10.21825/scad.v2i3.20543.

[41] Kim Y, Kim I, Kim J, Chung Y, Choi D. Evaluation of Surface Crack in Resistance Spot Welds of Zn-Coated Steel. Mater Trans 2014;55:171–5. https://doi.org/10.2320/matertrans.M2013244.

[42] Beal C, Kleber X, Fabrègue D, Mohamed B. Liquid zinc embrittlement of twinning-induced plasticity steel. Scr Mater 2012;66:1030–1033. https://doi.org/10.1016/j.scriptamat.2011.12.040.

[43] Kim YG, Kim IJ, Kim JS. Evaluation of surface crack in resistance spot welds of zn-coated steel. Mater Trans 2014;55:171–5. https://doi.org/10.2320/matertrans.M2013244.

[44] Ashiri R, Haque M, Ji C, Shamanian M, Salimijazi H, Park Y-D. Supercritical area and critical nugget diameter for liquid metal embrittlement of Zn-coated twining induced plasticity steels. Scr Mater 2015;109:6–10. https://doi.org/10.1016/j.scriptamat.2015.07.006.

[45] Jeon W, Sharma A, Jung JP. Liquid Metal Embrittlement of Galvanized TRIP Steels in Resistance Spot Welding. Metals (Basel) 2020;10:787–809.

[46] Beal C. Mechanical behaviour of a new automotive high manganese TWIP steel in the presence of liquid zinc. PhD Thesis 2012:1–187.

[47] Beal C, Kleber X, Fabregue D, Bouzekri M. Embrittlement of a high manganese TWIP steel in the presence of liquid zinc. Mater Sci Forum 2012;706–709:2041–6. https://doi.org/10.4028/www.scientific.net/MSF.706-709.2041.

[48] Jung G, Woo IS, Suh DW, Kim SJ. Liquid Zn assisted embrittlement of advanced high strength steels with different microstructures. Met Mater Int 2016;22:187–95. https://doi.org/10.1007/s12540-016-5579-7.

[49] Kang H, Cho L, Lee C, Cooman BC De. Zn Penetration in Liquid Metal Embrittled TWIP Steel. Metall Mater Trans A 2016;47:2885–905.

[50] Sierlinger R, Gruber M. A Cracking Good Story About Liquid Metal Embrittlement During Spot Welding of Advanced High Sterength Steels. 5th Int Conf Steels Cars Truck 2017:1–15.

[51] Ina K, Koizumi H. Penetration of liquid metals into solid metals and liquid metal embrittlement. Mater Sci Eng A 2004;s 387–389:390–394. https://doi.org/10.1016/j.msea.2004.05.042.

[52] Joseph B, Barbier F, Dagoury G, Aucouturier M. Rapid penetration of liquid Bi along Cu grain boundaries. Scr Mater 1998;39:775–81. https://doi.org/10.1016/S1359-6462(98)00230-9.

[53] Sigler D, Schroth J, Yang W, Gayden XQ, Jiang C, Sang Y, et al. Observations of liquid metal assisted cracking in resistance spot welds of zinc-coated advanced high strength steels. Sheet Met Weld Conf XIII 2008.

[54] D.-Y. Choi, S.-H. Uhm, C.M. Enloe, H. Lee, G. Kim CH. Liquid Metal Embrittlement of Resistance Spot Welded 1180TRIP Steel- Effects of Crack Geometry on Weld Mechanical Performance. Mater Sci Technol 2017;454–462. https://doi.org/https://doi.org/10.7449/2017/MST.

[55] D C, A S, JP J. Parametric study for liquid metal embrittlement. Sheet Met. Weld. Conf. XVIII. Am. Weld. Soc. Livonia, MI, 2018, p. 1–9.

[56] Siar O, Benlatreche Y, Dupuy T, Dancette S, Fabrègue D. Effect of Severe Welding Conditions on Liquid Metal Embrittlement of a 3rd-Generation Advanced High-Strength Steel. Metals (Basel) 2020;10:1166. https://doi.org/10.3390/met10091166.

[57] Choi D-Y, Sharma A, Uhm S, Jung J. Liquid Metal Embrittlement of Resistance Spot Welded

1180 TRIP Steel: Effect of Electrode Force on Cracking Behavior. Met Mater Int 2018;25. https://doi.org/10.1007/s12540-018-0180-x.

[58] Choi DY, Sharma A, Jung JP. Parametric Study for Liquid Metal Embrittlement in Resistance Spot Welds of Galvanized TRIP Steel,. Sheet Met. Weld. Conf. XVIII, 2018, p. 1–9.

[59] DiGiovanni C, He L, Pistek U, Goodwin F, Biro E, Zhou NY. Role of spot weld electrode geometry on liquid metal embrittlement crack development. J Manuf Process 2020;49:1–9. https://doi.org/10.1016/j.jmapro.2019.11.015.

[60] Benlatreche Y, Ghassemi-Armaki H, Duchet M. Spot-Weld integrity of Zn-coated 3rd Gen. advanced high strength steels in presence of LME. Int. Automot. Body Congr. IABC 2017 DEARBORN - Pap., 2017, p. 9–18.

[61] Wintjes E, DiGiovanni C, He L, Biro E, Zhou NY. Quantifying the link between crack distribution and resistance spot weld strength reduction in liquid metal embrittlement susceptible steels. Weld World 2019;63:807–14. https://doi.org/10.1007/s40194-019-00712-5.

[62] Benlatreche Y, Dupuy T, Ghassemi-Armaki H, Lucchini L. Methodology for Liquid Metal Embrittlement (LME) evaluation of coated steels during spot welding. 72nd Annu. Assem. Int. Inst. Weld., Bratislava, Slovakia: 2019, p. III-1959-19M.

[63] Barthelmie J, Schram A, Wesling V. Liquid Metal Embrittlement in Resistance Spot Welding and Hot Tensile Tests of Surface-refined TWIP Steels. Mater. Sci. Eng. Conf. Ser., vol. 118, AA(Technical University of Clausthal, Germany), AB(Technical University of Clausthal, Germany), AC(Technical University of Clausthal, Germany): 2016, p. 12002. https://doi.org/10.1088/1757-899X/118/1/012002.

[64] Ling Z, Wang M, Kong L, Chen K. Towards an explanation of liquid metal embrittlement cracking in resistance spot welding of dissimilar steels. Mater Des 2020;195:109055. https://doi.org/10.1016/j.matdes.2020.109055.

[65] Kim YG, Kim IJ, Kim JS, Chung Y Il, Choi DY. Evaluation of surface crack in resistance spot welds of zn-coated steel. Mater Trans 2014;55:171–5. https://doi.org/10.2320/matertrans.M2013244.

[66] Böhne C, Meschut G, Biegler M, Rethmeier M. Avoidance of liquid metal embrittlement during resistance spot welding by heat input dependent hold time adaption. Sci Technol Weld Join 2020;0:1–8. https://doi.org/10.1080/13621718.2020.1795585.

[67] Siar O, Dancette S, Dupuy T, Fabrègue D. Impact of liquid metal embrittlement inner cracks on the mechanical behavior of 3rd generation advanced high strength steel spot welds. J Mater Res Technol 2021;15:6678–89. https://doi.org/10.1016/j.jmrt.2021.11.100.

[68] Barthelmie J, Schram A, Wesling V. Liquid Metal Embrittlement in Resistance Spot Welding and Hot Tensile Tests of Surface-refined TWIP Steels. IOP Conf Ser Mater Sci Eng 2016;118. https://doi.org/10.1088/1757-899X/118/1/012002.

[69] Böhne C, Meschut G, Biegler M, Frei J, Rethmeier M. Prevention of liquid metal embrittlement cracks in resistance spot welds by adaption of electrode geometry. Sci Technol Weld Join 2020;25:303–10. https://doi.org/10.1080/13621718.2019.1693731.

[70] Murugan SP, Mahmud K, Ji C, Jo I, Park Y Do. Critical design parameters of the electrode for liquid metal embrittlement cracking in resistance spot welding. Weld World 2019;63:1613–32. https://doi.org/10.1007/S40194-019-00797-Y/FIGURES/21.

[71] Dupuy T. A novel electrode tip geometry to mitigate liquid metal embrittlement during resistance spot welding. Weld World 2022. https://doi.org/10.1007/s40194-022-01343-z.

[72] Barber B, Pearson K, Shojaee M, Midawi ARH, Sherepenko O, Ghassemi-Armaki H, et al. Comparative Analysis of Liquid Metal Embrittlement Reduction Methods in Zinc-Coated Third Generation Advanced High-Strehttps://uwaterloo.ca/faculties-academics/ngth Steels. Sheet Met Weld Conf XIX 2021:2A – 4.

[73] Bhattacharya D. Liquid metal embrittlement during resistance spot welding of Zn-coated high-strength steels. Mater Sci Technol (United Kingdom) 2018;34:1809–29. https://doi.org/10.1080/02670836.2018.1461595.

[74] DiGiovanni C, Shojaee M, Biro E, Zhou NY. Effect of External Loading on Liquid Metal Embrittlement Severity during Resistance Spot Welding. Manuf Lett 2022;33:11–4. https://doi.org/10.1016/j.mfglet.2022.06.003.

[75] DiGiovanni C. Liquid metal embrittlement in resistance spot welding: The thermomechanical origin and embrittler transport mechanism. 2021.

[76] Pearson K, Barber B, Shojaee M, Midawi ARH, Sherepenko O, Ghassemi-armaki H, et al. Industrially Viable Methods To Reduce Liquid Metal Embrittlement Severity in Resistance Spot-Welded Third-Generation Advanced High-Strength Steels 2021:1–12.

[77] Abdul Karim M, Park Y-D. A Review on Welding of Dissimilar Metals in Car Body Manufacturing. J Weld Join 2020;38:8–23. https://doi.org/10.5781/jwj.2020.38.1.1.

[78] ASTM E8. ASTM E8/E8M standard test methods for tension testing of metallic materials 1. Annu B ASTM Stand 4 2010:1–27. https://doi.org/10.1520/E0008.

[79] Kasuya T, Yurioka N. Carbon Equivalent and Multiplying Factor for Hardenability of Steel. Weld Res Suppl 1993:263-s-268-s.

[80] Shojaee M, Midawi ARH, Barber B, Ghassemi-Armaki H, Worswick M, Biro E. Mechanical properties and failure behavior of resistance spot welded third-generation advanced high strength steels. J Manuf Process 2021;65:364–72. https://doi.org/10.1016/j.jmapro.2021.03.047.

[81] American Welding Society. AWS D8.1M, 3rd Edition, 2021 - Specification for Automotive Weld Quality Resistance Spot Welding of Steel, ISBN:978-1-64322-178-6 2021.

[82] Ambroziak A, Korzeniowski M. Using resistance spot welding for joining aluminium elements in automotive industry. Arch Civ Mech Eng 2010;10:5–13. https://doi.org/10.1016/s1644-9665(12)60126-5.

[83] Cho Y, Rhee S. Experimental Study of Nugget Formation in Resistance Spot Welding Nugget formation mechanism and its effect on the welding process parameters are observed by using a digital high-speed camera. n.d.

[84] Frei J, Biegler M, Rethmeier M, Böhne C, Meschut G. Investigation of liquid metal embrittlement of dual phase steel joints by electro-thermomechanical spot-welding simulation. Sci Technol Weld Join 2019;24:624–33. https://doi.org/10.1080/13621718.2019.1582203.

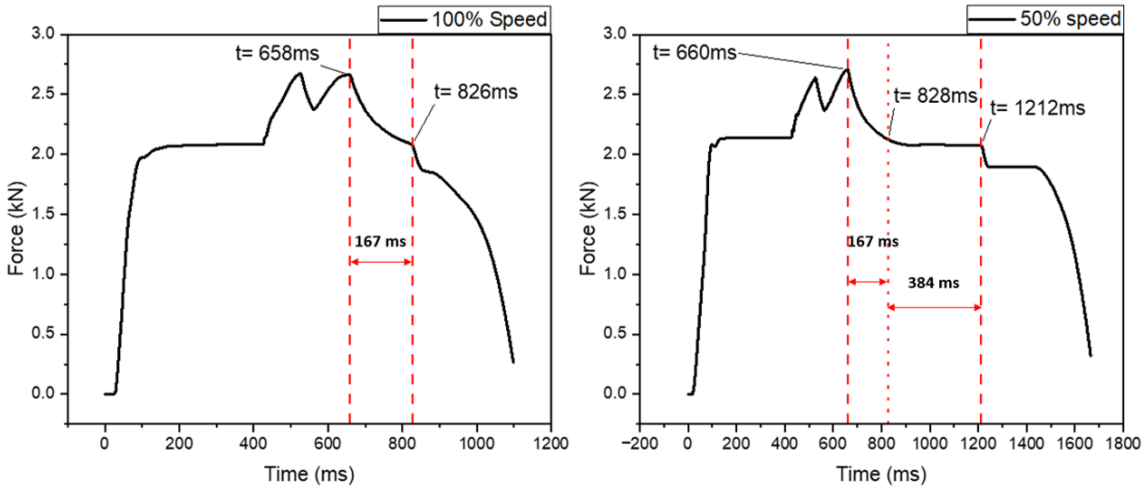
[85] Frei J, Rethmeier M. Susceptibility of electrolytically galvanized dual-phase steel sheets to liquid metal embrittlement during resistance spot welding. Weld World 2018;62:1031–7. https://doi.org/10.1007/s40194-018-0619-1.

[86] DiGiovanni C, He L, Hawkins C, Zhou NY, Biro E. Significance of cutting plane in liquid

metal embrittlement severity quantification. SN Appl Sci 2021;3. https://doi.org/10.1007/s42452-021-04608-2.

[87] Choi DY, Uhm SH, Enloe CM, Lee H, Kim G, Horvath C. Liquid metal embrittlement of resistance spot welded 1180TRIP steel - Effects of crack geometry on weld mechanical performance. Mater. Sci. Technol. Conf. Exhib. 2017, MS T 2017, vol. 1, Association for Iron and Steel Technology, AISTECH; 2017, p. 454–62. https://doi.org/10.7449/2017/MST_2017_454_462.

Appendix



All the experiments for effect of pre-strain on LME were done on 50% welding robot speed to avoid slippage of the electrodes which changes the hold time on the robot timer. Graph above shows the extension of hold time by 384 ms when using 50% of the robot speed. Graphs were produce by in-situ force measurement.